Zeitschrift: Helvetica Physica Acta

Band: 67 (1994)

Heft: 2

Vereinsnachrichten: Réunion de printemps de la Société Suisse de Physique = Frühjahrstagung der Schweizerischen Physikalischen Gesellschaft = Spring meeting of the Swiss Physical Society

Autor: [s.n.]

Réunion de Printemps de la Société Suisse de Physique

Frühjahrstagung der Schweizerischen Physikalischen Gesellschaft

Spring Meeting of the Swiss Physical Society

March 17 and 18, 1994

Bern, Switzerland

Helv Phys Acta
Vol. 67 (1994)

0018-0238/94/020203-34$1.50+0.20/0

Insulating Phase of Mercury in Cold-Deposited Films

A. V. Danilov[1], S. E. Kubatkin[1], I. L. Landau[1,2], I. A Parshin[1] and L. Rinderer[2]

[1] Kapitza Institute for Physical Problems, 117334 Moscow, Russia
[2] Institut Physique Experimentale, Université de Lausanne, 1015 Lausanne, Switzerland

We present experimental evidences that mercury forms a metastable insulating phase in films condensed on glass substrates at low temperatures. This phase exists in films only up to some critical thickness $d_c \approx 60$ Å. Our results cannot be explained by the assumption that films have an islands structure. We believe that similar phases exist also in quench-condensed lead films and, may be, in some other metals. The possibility that disordered system of metallic atoms can form an insulator has never been considered.

A usual way to produce disordered metallic films is a deposition at low temperatures. The conductivity onset in most of such films corresponds to a very low film thickness d ~ 10Å. However, there exist some metals (Pb, Hg and a few others) which have a finite conductivity only if $d > d_c \approx$ 60-80 Å (see [1-3] and references therein). The commonly accepted explanation is that these films consist of isolated islands. An increase in d above d_c closes gaps and makes the film continuous.

We are sure that it is not the case. The actual reason is that these metals form metastable insulating phases at low temperatures. The most probable reason for the insulating behavior is the low film density. An increase in the thickness causes the transition to a more dense conducting state. This transition is similar to that observed in some of amorphous metals when the film growth leads to a transition to crystalline phases (see [4] and references therein). We consider the situation in Hg films as absolutely the same with the only exception that the metastable amorphous phase of Hg is an insulator. Some new experimental results presented here definitely support our idea.

The main results: (1) Films with d slightly above d_c shows a steep irreversible decrease of the resistance at very low temperatures (curve 1 in Fig. 1 corresponds to the film with $d = d_c + 4$Å). (2) If d is below but very near to d_c it is possible to cause the transition to the conducting state by the temperature rise (curve 2 in Fig. 1 shows the annealing of the film with $d = d_c - 1$Å). (3) The film with $d = 49\text{Å} \approx d_c - 10\text{Å}$ has shown no conductivity in spite of the annealing it up to T= 95K. After this annealing the substrate was cooled down back to T= 4.2K and we had to evaporate additional 43Å of Hg for the conductivity onset. (4) The critical thickness for the conductivity onset at T= 38K $d_c(38\text{K}) = 42$Å is sufficiently smaller than $d_c(4.2\text{K}) \approx 60$Å. (5) Resistance jumps of different amplitudes have been observed during the film annealing (a few jumps can be seen in Fig. 1). During the largest one a decrease in the film resistance was more than two orders of magnitude. (6) The temperature rise above T≈110 K caused an increase in the film resistance (see insert

to Fig. 1). The further temperature rise led to a disappearance of the film conductivity.

All the results can be explained by the idea that we are dealing with the metastable insulating phase of Hg. In this model a sharp decrease of the film resistance during the annealing reflects a thermally activated transition to the conducting state. The appearance of the conductivity during the deposition can be attributed to a similar transition caused by a kinetic energy of condensing atoms.

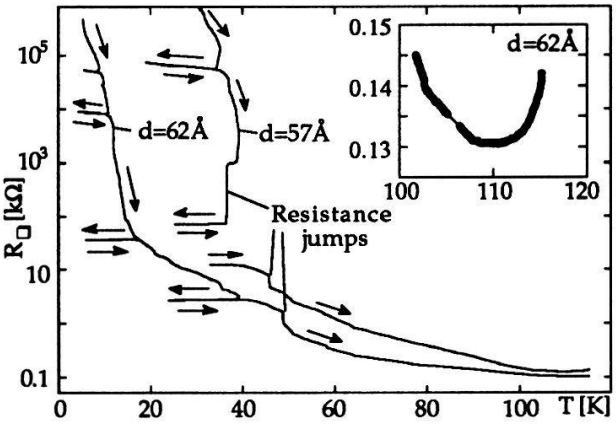

Fig. 1. The film resistance versus temperature for two films with different thicknesses. Insert shows the high temperature behavior.

The transition caused by the deposition should begin near the film surface and it is to increase the film density due to a momentum of incident atoms towards the substrate. A different situation arises during the annealing. In this case a transition can happen in the limited region inside the film. The only way to increase the density in some region is to decrease it outside. This process should enlarge the density fluctuations across the film. In thin films it can cause the film disintegration because almost all the material will concentrate in separate clusters. This kind of the annealing is responsible for the experimental result (6). In more thin films the disintegration can begin before the transition to the conducting state. It can explain result (3) when the film with d= 49Å has shown no conductivity up to T= 95K. The insulating phase of Hg was formed again between clusters during the extra deposition. We consider it as the only possible explanation that we had to deposit additional 43Å of Hg for the conductivity onset.

If the metastable insulating phase of Hg do exist in cold deposited films, an increase in the substrate temperature during the deposition should promote the transition to the conducting state. This simple idea is in a complete agreement with the experimental result (4).

A transition from the metastable to the equilibrium state should be accompanied by the film heating due a to release of the latent heat. This heating can accelerate the transition near-by and cause an avalanche. The most probable that in disordered films avalanches will happen in the limited film area. We believe that such limited avalanches is the reason for the resistance jumps (5).

References

[1] E. T. S. Appleyard and J. R. Bristow, Proc. Phys. Soc. A, **172**, 530 (1939).

[2] M. Strongin et al. Phys. Rev. B **1**, 1078 (1970).

[3] V. L. Tsymbalenko and A. I. Shal'nikov, Sov. Phys. JETP **38**, 1043 (1974).

[5] V.M. Kuz'menko, V.I. Mel'nikov and V.A. Rakhubovskii Sov. Phys. JETP **59**, 612 (1984).

Spin-Wave Patterns and Spin-Wave Turbulence[1]

F.J. Elmer

Institut für Physik, Universität Basel, 4056 Basel

The dynamics of spin waves is studied analytically and numerically at the onset of the parallel pumping instability of a ferromagnetic film.

Parametric excitation of spin waves is well-known since forty years [1]. Almost nothing is, however, known about the spatial patterns of the magnetization built up by the parametrically exited spin waves. In order to reduce the generally three-dimensional patterns to quasi-two-dimensional ones (which will be easier to visualize) it is convenient to study films.

We investigate an infinitely extended, insulating ferromagnetic film of thickness d. It is subjected to a uniform static magnetic field H perpendicular to the plane of the film, being strong enough to saturate the film in one single domain. The driving field $h\cos\omega t$ is assumed to be uniform and parallel to the static field (parallel pumping). From bulk calculations it is well-known that the most unstable modes are spin waves with $\omega_k = \omega/2$ travelling perpendicular to the magnetic field [1]. At the instability threshold h_c all unstable spin waves have the same critical wave number k_c but propagate in different directions within the plane of the film. Near the threshold the complex amplitudes A_j of pairs of standing spin waves with wave vector $\vec{k}_j = \pm k_c(\cos\alpha_j \cdot \vec{e}_x + \sin\alpha_j \cdot \vec{e}_y)$ are governed by a set of coupled Landau equations [2]:

$$\tau_0 \frac{dA_j}{dt} = \epsilon A_j - c\left[|A_j|^2 + \sum_{l\neq j} a(\alpha_l - \alpha_j)|A_l|^2\right] A_j, \qquad (1)$$

where $\epsilon = (h - h_c)/h_c$, τ_0 and c are positive constants characterizing typical scales for time (i.e. τ_0/ϵ) and amplitudes (i.e. $\sqrt{\epsilon/\tau_0}$), respectively. The dynamical behaviour is determined by the coupling function a only which is a π-periodic function because of rotational symmetry. It is not an even function, because the magnetic field strongly breaks the reflection symmetry. Thus, oscillations in time are expected [2]. We have calculated a numerically.

Stationary patterns are built up by N different standing waves. For $N = 1$ and $N > 4$ all patterns are linearly unstable. For $k_c d \ll 1$ only squares and quasiperiodic patterns with $N = 3$ and $|\alpha_i - \alpha_j| < \pi/2$ (see Fig. 1) are stable. At $k_c d \approx 0.1$ the squares and the quasiperiodic patterns become unstable. In our simulation of (1) 48 amplitudes were included. For $k_c d > 0.1$ the system starts to oscillate. After some chaotic transients it reaches a regular heteroclinic orbit connecting several unstable wave patterns. Heteroclinic orbits make the system extremely sensitive to thermal noise leading to a kind of turbulence characterized by random switching between different wave patterns (see Fig. 2). The mean switching time decreases with the noise amplitude. The trend is to rotate patterns by some finite angle. This is a reminiscence of some heteroclinic orbit. A similar scenario of turbulence

[1]This work was supported by the Swiss National Science Foundation.

was proposed and experimentally verified for rotating Rayleigh-Bénard convection [3]. At the onset of convection this system is also governed by (1) with $a(-\Delta\alpha) \neq a(\Delta\alpha)$.

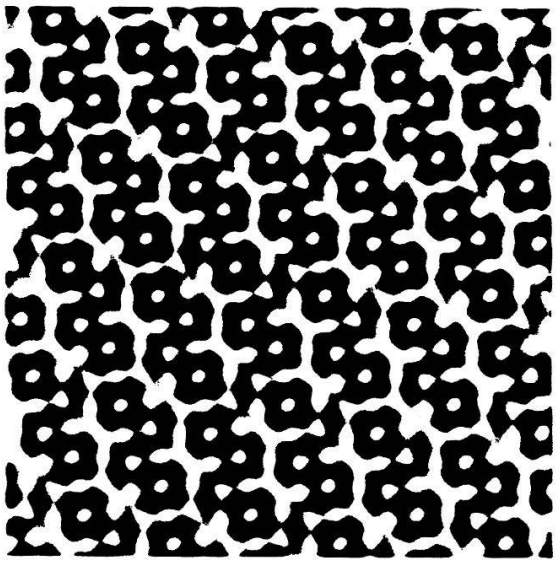

Figure 1: Quasiperiodic pattern calculated for $k_c d \to 0$. The angles are $\alpha_3 - \alpha_2 = \alpha_2 - \alpha_1 = 0.7$. The greyscale codes the deviation of the temporal average of the component of the magnetization perpendicular to the film from its thermal equilibrium value. Black means no deviation. Such an image would be expected in an experiment using Faraday rotation as a visualization technique.

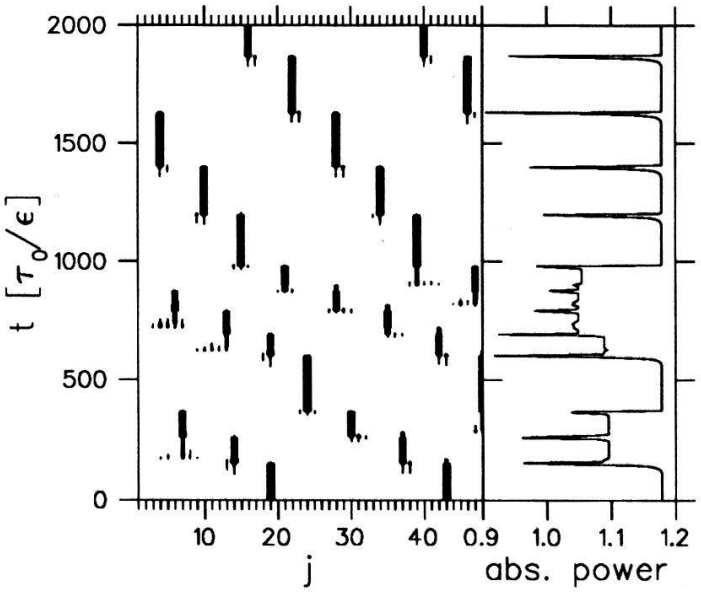

Figure 2: Simulation with white noise (noise amplitude 10^{-8}) and 48 amplitudes. The width of the vertical bars codes $|A_j|$. The absorbed power is measured in arbitrary units. System parameters: $d = 20$ exchange length units, $\omega = 0.4 \cdot 4\pi\gamma M_0$, $H = 1.1 \cdot 4\pi M_0$, where γ is the gyromagnetic ratio and M_0 the thermal equilibrium value of the magnetization. These parameters lead to $k_c d = 0.784$. Dissipation expressed in terms of the relative linewidth of the ferromagnetic resonance line is 0.002.

References

[1] For a review see R. W. Damon, in *Magnetism*, Vol. 1, edited by G.T. Rado and H. Suhl (Academic Press, New York, 1963).
[2] F.J. Elmer, Phys. Rev. Lett. **70**, 2028 (1993).
[3] F.H. Busse and K.E. Heikes, Science **208**, 173 (1980).

FREEZING OF SUPERCOOLED REFRACTORY METALS

V. Soares, D. Houch, L. Rinderer
Institute of Experimental Physics, University of Lausanne
CH-1015 – Lausanne, Switzerland

Employing the Stefan model we investigate the solidification of droplets of refractory metals near the limit of stability of the metastable liquid. We present an expression for the amount of supercooling a metal droplet may sustain before nucleation of the crystalline phase from their melt and this model provides a qualitative explanation to the large supercoolings which we have observed in different metals as W, Ta, Nb, and Mo.

1. Introduction.

It is known that a supercooled state of the high-temperature phase can be obtained in a first-order phase transition. This metastable state is stable within certain limits, but sooner or later goes over into a phase that is stable at a given temperature T_{limit} by formation and subsequent growth centres of this phase. This temperature T_{limit} define the amount of supercooling $\Delta T = T_M - T_{limit}$ the liquid can sustain and, then, control the rate of the relaxation of the metastable state. It has been observed that at very large supercoolings the liquid transforms into glass but pure metals has always been crystallised before to attain this state.

In this paper we consider the conditions for the appearance of a limit for the observed instability of the liquids by using the Stefan model of solidification. In this model, the velocity of the growth is determined by the competition between the heat release at the interface solid-liquid and the heat dissipation in the liquid phase. We present an analysis of this instability and these results are compared to those obtained from the quenching of liquid droplets of refractory metals.

2. Experimental procedure and the Stefan model of solidification.

It has been possible to observe in stereophotographic images of free falling submillimeter liquid refractory metals the thermal history of these droplets.[1] With knowledge of the drop release temperature and the free-fall time to solidification, the temperature at which nucleation occurs and the supercooling of the droplets can be determined. The experiment is performed in glass chamber filled with pure He. The discharge of condenser melts the metal wire and produces the droplets that are ejected into the chamber. They describe free-fall trajectories and are cooled during the time of fall.[2]

The Stefan model of solidification considers a *supercooled liquid* at temperature T_{init} lower than T_M and occupying the whole space. At time $t=0$ nucleation occur and we examine the case of nucleation at a single point. Then, a spherical front $r=R(t)$ of the solid nucleus will begin propagating from $r=0$. One ignores the Gibbs-Thomson effect by assuming freezing at temperature T_M. If the thermal properties of the solid and the liquid are assumed to be the same, the solution of the equation of heat gives an analytical function[3] to the distribution of temperature inside the liquid as

$$T(r,t) = T_{init} + \frac{2\lambda(T_M - T_{init})}{e^{-\lambda^2} - \lambda\sqrt{\pi}erfc(\lambda)}\left[\frac{\sqrt{\alpha_L t}}{r}e^{-\frac{r^2}{4\alpha_L t}} - \frac{\sqrt{\pi}}{2}erfc\left(\frac{r}{2\sqrt{\alpha_L t}}\right)\right] \qquad (1)$$

when the interface liquid-solid $R(t)$ obeys

$$R(t) = 2\lambda\sqrt{\alpha_L t}, \qquad t > 0 \qquad (2)$$

where α_L is the diffusivity of the liquid phase. We determine λ by the root of the equation

written below, obtained from the heat-balance conditions at the interface solid-liquid:

$$2\lambda^2 e^{\lambda^2}\left[e^{-\lambda^2} - \lambda\sqrt{\pi}erfc(\lambda)\right] = St_{init}, \qquad St_{init} = \frac{c_L(T_M - T_{init})}{L} \tag{3}$$

The constants c_L and L are the specific heat and the latent heat of the liquid phase of the material. St_{init} is defined as the Stefan number due to the initial conditions of the solidification and erfc(λ) is the complementary of the error function erf(λ).

3. Results and conclusions.

The solution of the heat-balance equation to λ has interest only to real and positive λ. In this way, the solid phase grows at the interior of the liquid state. In this case, the values of St must remain between 0 and 1.[4] From the St number behavior, we can define, then, a minimum value to the initial temperature T_{init} of the liquid phase at the beginning of the solidification process. Therefore, it establishes a limit temperature T_{limit} to the metastability of the liquid phase:

$$\frac{T_{init}}{T_M} > 1 - \frac{L}{c_P T_M}, \qquad \frac{T_{limit}}{T_M} = 1 - \frac{L}{c_P T_M} \tag{4}$$

We compare our results to this limit predicted by Stefan model in the figure. The large supercoolings observed in the refractory metals and, therefore, the limit temperature to the metastability of these liquids (black squares ■) agrees with the predictions of the model (straight line —). However, the model fails to explain the much larger supercoolings observed in metals with low melting point (white squares □). The approximations made of equal specific heat and densities in both phases surely contribute to this discrepancy. Nevertheless, this model gives a qualitative idea of the solidification process and establishes a thermal limit for the metastability of the liquid phase. This limit depends only on pure thermodynamic parameters as the specific heat, the latent heat and the melting temperature of the sample. The behavior of the limit temperature for the metastability of liquid metals with low melting point suggest that we should expect to observe much larger supercoolings to refractory metals than those presented in this report.

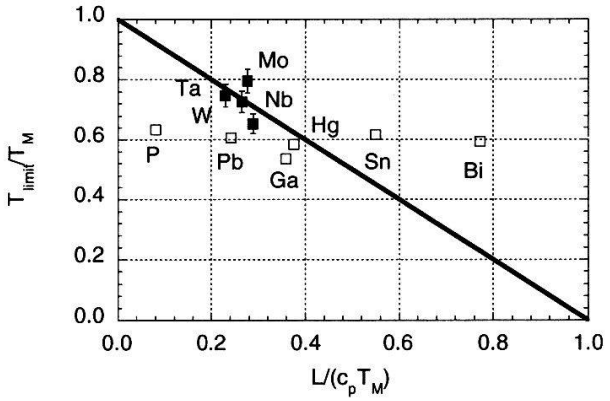

ACKNOWLEDGMENT.

We thank the assistance of Mr. Rossier with the photographs and the support from FNRS.

References

[1] V. Soares, L. Rinderer and E. Meyer, *Mat. Sci. Eng., A32 (1991) 711*
[2] E. Meyer and L. Rinderer, *J. Crystal Growth, 28 (1975) 199*
[3] H. S. Carslaw and J. C. Jæger, Conduction of Heat in Solids, p.295
[4] V. Alexiades and A. D. Solomon, Mathematical Modeling of Melting and Freezing Process, p.119.

THE EXPONENTIAL CRITICAL STATE OF HIGH-Tc CERAMICS

H. Castro[1], B. Fluckiger,[1] J.-F. Loude[2], E. Holguin[3] and L. Rinderer[1]

1 Institut de Physique Expérimentale, Université de Lausanne, Switzerland
2 Institut de Physique Nucléaire, Université de Lausanne, Switzerland
3 Departamento de Física, Universidad del Cauca, Popayán - Colombia

The critical current in high-Tc materials is strongly reduced by a magnetic field. We studied this dependency for tubular YBCO samples. We find an exponential drop as the field is increased from zero up to some tens of oersted. This behavior was already observed by others, however little work has been done in this direction. We define what we call the 'exponential critical state' of HTSC and compare the prediction for the magnetization with experimental data. Furthermore, the 'Kim critical state' is obtained as the small field limit.

INTRODUCTION

One of the most disappointing characteristics of the high-Tc ceramics which limits its range of applications is the important decrease in the critical current when the sample is exposed to a magnetic field. Their structure, made of grains interconnected by weak links, is responsible for this behavior. Nonetheless, the phenomenological model of Kim [1], originally developed for Type II 'hard superconductors', was successfully applied to interpret the magnetic response and particularly, the a.c. susceptibility measurements [2]. This theory postulates a field dependence of the critical current of the form

$$J_c(B) = \frac{\alpha}{B_0 + B} \qquad (1)$$

where α and B_o are material and temperature dependent parameters and B, the magnetic induction. However, this law is only an approximate one as becomes evident after looking at the experimental data of several authors.

Here we present measurements of the transport critical current in $(Y_1Ba_2Cu_3O_{7-\delta})_{1-x}Ag_x$ sintered samples as function of magnetic field and show that an exponential law fits these results. We define a 'critical state' in the same way as originally done by Kim [1], and compute the magnetization curve. Finally, we show that Kim's 'critical state' is a good approximation for low fields, as is the case in typical a.c. susceptibility measurements.

CRITICAL CURRENT

We measure the critical current by the d.c. four contacts method with a 1 μV criterion. We first immerse the sample in a liquid nitrogen bath, then apply a static magnetic field parallel to the tube axis. We explore the field range in which the shielding properties are still important, i.e. for fields smaller than the second critical field of the Josephson medium H_{c2J}, about 60 Oe.

Figure 1 shows the results for samples with different Ag weight fraction x. All of them follow an exponential behavior and are fitted with the three-parameters law

$$J_c(B) = J_{co} \cdot \exp\left(-B / B_o\right) + J_{c1} \qquad (2)$$

The current component J_{c1} decreases slowly and disappears only at fields above the grain's second critical field H_{c2g}, of the order of 10^5 Oe. It is taken as constant in this case.

Table I shows the values of the parameters obtained from the fit.

Table I Param. values for YBCO-Ag samples

x	J_{co}(A/cm^2)	J_{c1}(A/cm^2)	B_o (G)
0	148.7	5.13	19.6
0.2	78.1	12.2	18.9
0.3	64.0	18.7	17.7

THE EXPONENTIAL CRITICAL STATE

In fig. 2 we plot the trapped induction B_i vs. the applied one B_e, for $x = 0.3$. The details of this measurements are published elsewhere [3].

The infinite set of possible equilibrium states define a continuous curve called the 'critical state'. The corresponding equation is obtained by integrating Ampere's law from an arbitrary radius r to the outer one a, using eq. 2 for the current. In this way we obtain the radial dependence of the magnetic induction inside the sample's wall as

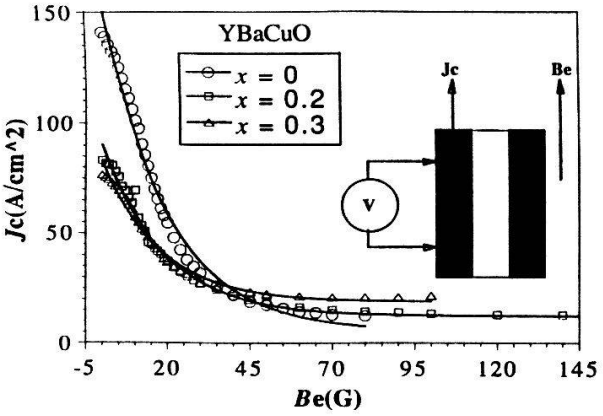

Fig. 1 Critical current vs. external field

$$B(r) = B_0 \cdot \ln\left\{\exp\left[b_e - \left(\frac{a-r}{w}\right)b_1\right] + \left(\frac{J_{c0}}{J_{c1}}\right)\cdot\left[\exp\left[-\left(\frac{a-r}{w}\right)b_1\right]-1\right]\right\} \qquad (3)$$

where $b_e = B_e / B_0$, $b_1 = w \cdot J_{c1} / B_0$ and w is the wall thickness of the sample (1 mm).

Eq. 3 allows us to evaluate the shielding field B^*, that is the maximum screenable field in the hole, by making $B(r = a-w) = 0$ and then solving for $B_e = B^*$.

In a similar way we find the trapped field as function of the applied one by putting $r = a-w$:

$$B_i = B_0 \cdot \ln\left\{\exp(b_e - b_1) + \left(\frac{J_{c0}}{J_{c1}}\right)\cdot\left[\exp(-b_1)-1\right]\right\} \qquad (5)$$

The solid line in fig. 2 is given by a fit of the experimental data to eq. 5. The dashed line is a fit to Kim's model and, for comparison purposes, the dotted line is obtained from Bean's model. There seems not to be a big difference between the exponential and Kim's fit. However the former gives parameter values nearer to those from table 1. Similar results are obtained with samples with different x.

Expanding into a series the expression for J_c as given by eq. 2, retaining only the first two terms and neglecting J_{c1}, we obtain for $B << B_0$,

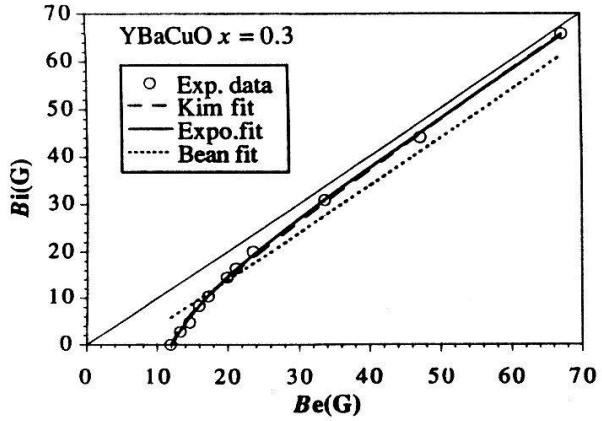

Fig. 2 Trapped vs. applied field at 77K

$$J_c(B << B_0) \approx J_{c0}\cdot\left[1 - \frac{B}{B_0}\right] \approx \frac{J_{c0}\cdot B_0}{B_0 + B} \qquad (6)$$

giving for the low field limit the same form as eq. 1.

ACKNOWLEDGMENTS

We thanks Dr. V. Soares for fruitful discussions.

This work was partially supported by the Swiss National Science Foundation.

REFERENCES

[1] Y. B. Kim, C. F. Hempstead and A. R. Strnad, Phys. Rev. Lett. **9** (1962) 306

[2] H. K. Müller, *Physica C* **168** (1990) 585

[3] H. Castro et al., to appear in the proceedings of the LT20 Conference, Eugene 4-11 Aug. 93

In situ DC-Hydrogen Plasma Cleaning of Si(111) Surfaces

U. Kafader, H. Sirringhaus, J. Ramm*, A. Dommann# and H. von Känel
Laboratorium für Festkörperphysik, ETH Zürich, CH-8093 Zürich,
*BALZERS AG, FL-9496Balzers, #Neu-Technikum Buchs, CH-9470 Buchs

A DC hydrogen/argon plasma generated in a plasma module coupled to a MBE/STM-system is used for *in situ* silicon substrate cleaning. The removal of the native oxide and carbon contamination is monitored by XPS. RHEED and STM observations indicate surface roughening by the plasma process of the order of 10-50 Å on a vertical scale and several 100Å on a lateral scale, respectively. The quality of homoepitaxial silicon layers grown on the plasma cleaned surface is investigated by high-resolution XRD and defect-etching. The results are compared to those achieved with traditional cleaning techniques.

The cleaning of silicon wafers is an important step in microelectronic device fabrication. Different methods such as thermal desorption, wet chemical etching, and dry plasma etching have been applied to remove the native oxide and carbon contaminants. In contrast to most plasma etching facilities using a RF-excited plasma we are working with a Balzers DC plasma cleaning module similar to the one described in reference 1. The plasma chamber is mounted on the existing MBE machine equipped with the following *in situ* analysing tools: RHEED, UPS, XPS and STM.

The three inch silicon wafers (Unisil, (111)-orientated, n-type, 0.75-1.0 Ωcm) are introduced into the system as obtained from the manufacturer and outgassed at 550°C. The sample is grounded during the etching process at a H_2/Ar flow of 18sccm/18sccm resulting in a chamber pressure of typically $6 \cdot 10^{-3}$mbar. The plasma discharge voltage is 25V.

After a 10 minute plasma exposure the native oxide of the wafer is completely removed as seen by the absence of the O1s core level in XPS. No carbon contamination can be detected. In the UPS spectra the typical surface states of the 7x7 reconstruction between the Fermi-level and 2eV binding energy are completely absent (fig. 1). Instead features atributed to Si-H and Si-H_2 species can be found in the 5 to 9 eV binding energy range [2]. The RHEED diagrams of the etched surfaces exhibit intense three dimensional spots indicating some surface roughness. This is more quantitatively confirmed by STM observations showing a peak to peak roughness up to 50Å on a lateral scale of the order of 200Å (fig. 2).

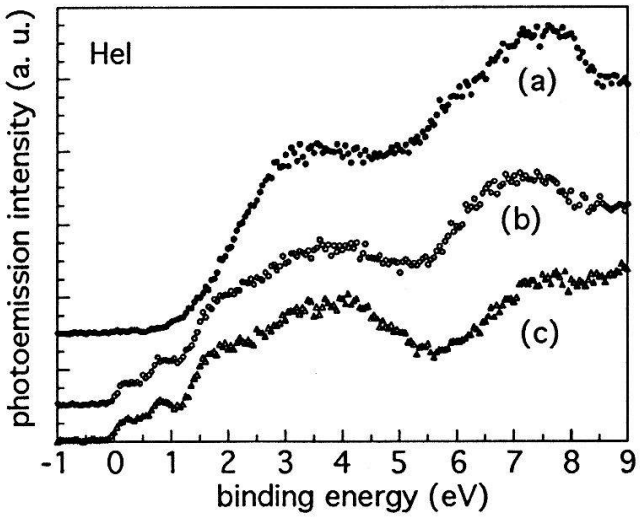

Fig.1: UPS spectra of the Si(111) surface taken after the plasma cleaning (a), after annealing of the cleaned surface at 550°C (b) and of the clean 7x7 reconstructed surface (c).

Upon annealing the hydrogen desorption between 200°C and 500°C can be followed by monitoring the increase of the hydrogen partial pressure. In the RHEED diagram the three dimensional spots disappear around 400°C and first weak traces of the 7x7 reconstruction can be detected at 450°C already. Although the RHEED intensity is rather low, the UPS spectrum after an anneal at 550°C shows the typical surface states of the 7x7 reconstructed surface (fig. 1). At about 5-7 eV however, some intensity of hydrogenated Si remains visible.

A technological important point is the suitability of the plasma cleaned surface for homoepitaxial growth. For this purpose we have grown typically 4000Å thick silicon layers at temperatures of 500°C, 600°C and 700°C and examined their crystalline quality by means of defect etching and high resolution XRD rocking curve experiments. The scattering intensity away from the Bragg position decreases with increasing growth temperature such that for 700°C there is hardly any difference to reference measurements on bare substrates. The stacking fault densitiy generally lies above $5 \cdot 10^7$ cm^{-2}. Transmission electron micrographs show that they are generated at the interface. Only for growth temperatures of 700°C defect densities as low as $3 \cdot 10^7$ cm^{-2} can be found.

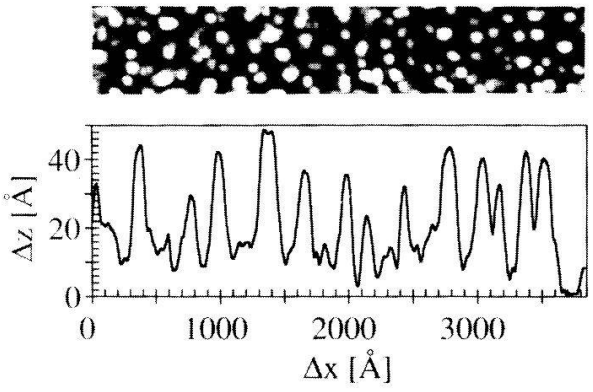

Fig.2: a) STM topograph after plasma cleaning, b) Cross section showing the surface roughness (Tip bias V_t=3V, tunneling current I_t=0.5nA),.

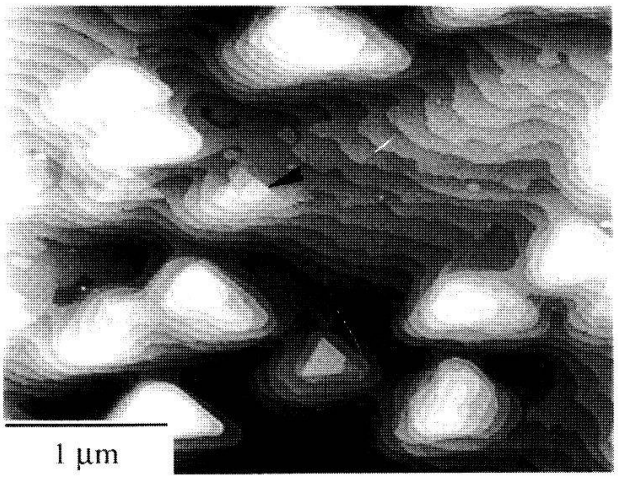

Fig.3: Large scale STM scan taken from a Si-buffer grown at 700°C showing step pinning at stacking faults (indicated by arrow) and screw dislocations. (V_t=-2V, I_t=0.5nA),.

Large-scale STM scans indicate that the bad crystalline quality of films grown at the lower temperatures is associated with a partially three dimensional growth mode, resulting in pyramid-shaped features with lateral dimensions of a few thousends of Å. At 600°C the pyramids are less extended and in between a step flow growth mechanism is observed. At 700°C the pure step flow regime is achieved, but step pinning at screw dislocations and stacking faults takes place (fig. 3). From the dimensions of the triangular shaped stacking fault areas we can conclude again that the stacking fault tetraeders nucleate at the interface.

The defect formation may have different sources. First, one can imagine residual contamination by oxygen or carbon in the plasma chamber or during sample transfer. Alternatively, the plasma process may lead to hydrogen incorporation into the substrate changing the lattice parameter and, hence favouring dislocation formation near the interface. In addition, one has to keep in mind, that the stacking fault formation energy is rather low on Si(111) surfaces. The results of Ramm *et al.* [3] obtained by similar experiments on the Si(100) surface strongly indicate that the reduction of contamination sources is particularly critical for obtaining silicon buffers with a low defect density.

Comparison of the results to those of layers grown on traditionally cleaned (thermal oxide desorption at 830°C under low silicon flux) silicon wafers or a combination of both methods show no clear differences in the defect density or in the surface morphology as observed by STM. However, post-growth annealing of the layers above the surface phase transition temperature of 830°C improved the 7x7 surface reconstruction considerably.

In conclusion, the most important parameters in homoepitaxial growth on Si(111) seem to be the growth temperature and the cleanliness of the surface and the MBE system. The DC plasma etching process may become an effective *in situ* method of surface cleaning, provided that post-plasma contamination can be further reduced.

[1] J. Ramm, E. Beck, A. Zueger, A. Dommann and R. E. Pixley, Thin Solid Films **228**, 23 (1993).
[2] J. J. Koulmann, F. Ringeisen, M. Alaoui and D. Bolmont, Phys. Rev. **B41**, 3878 (1990).
[3] J. Ramm., E. Beck, A. Dommann, I. Eisele, D. Krüger and G. Lippert, proc. GADEST '93, Chossewitz, Germany

Nonlinear Dynamics of Atomic Force Microscopes[1]

F.J. Elmer

Institut für Physik, Universität Basel, 4056 Basel

We study theoretically the dynamical behaviour of atomic force microscopes (AFM) in the regime of fast nonadiabatic scanning.

The cantilever of an atomic force microscope (AFM) [1] can be seen as a harmonic oscillator interacting via the tip with a corrugated surface. Its equilibrium position x_0 and resonance frequency ω_0 change due to the interaction. The cantilever turns into an anharmonic oscillator because the interaction is nonlinear.

What will happen if the AFM moves fast across the surface? Assuming a perfect periodic corrugation the scan transforms this spatial periodicity into a temporal periodicity with a frequency ω ("wash-board frequency") which is proportional to the scan velocity. First we expect that the periodic oscillation of the equilibrium position will lead to a strong resonance peak at $\omega = \omega_0$. But also weak resonance peaks at $\omega = \omega_0/n$ (n integer) are expected due to resonant excitations of higher harmonics of the anharmonic oscillation. The periodic oscillation of the resonance frequency leads also to parametric resonance at $\omega = 2\omega_0/n$ (n integer). It is well-known that damping suppresses parametric resonance. In order to get parametric resonance the amplitude of the frequency oscillation should exceed a threshold. The threshold increases with the damping constant and with the order n.

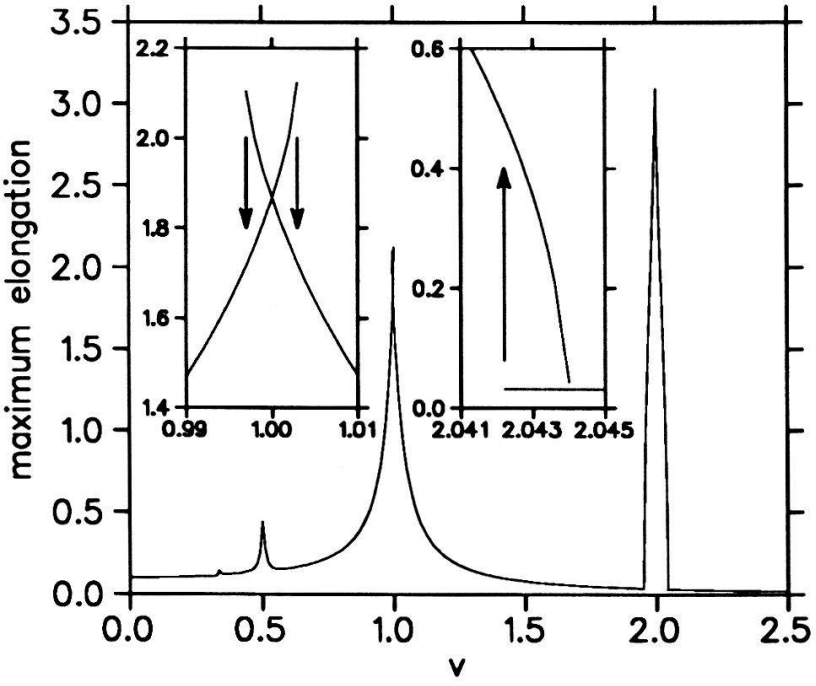

Figure 1: Maximum elongation x for $b = 0.1$ and $\gamma = 0.02$. The insets show bistability at the peak of the main resonance and at the right shoulder of the peak of the first-order parametric resonance.

[1]This work was supported by the Swiss National Science Foundation.

A simple dynamical model for an AFM is

$$\ddot{x} + \gamma \dot{x} + x = b \cos(x + v t), \tag{1}$$

where x is the elongation of the cantilever measured in units of the corrugation periodicity, γ is a phenomenological damping constant, b is the strength of the interaction, and v is the scan velocity. The time t is measured in units of $1/\omega_0$. Thus, v is the ratio of the wash-board frequency and the resonance frequency. The model has all the above mentioned features: It is nonlinear and the equilibrium position and the frequency vary in time since $\cos(x + vt) = \cos vt - \sin vt \cdot x + \mathcal{O}(x^2)$. The model can be seen as the equation of motion of the torsion mode of the cantilever in a friction force microscope.

Fig. 1 shows numerical calculations of the maximum elongation x as a function of the scan velocity v. The main resonance peak at $v = 1$ is clearly seen. The peaks of the second and third harmonic are also present at $v = 1/2$ and $v = 1/3$, respectively, but the strongest and sharpest peak comes from the first-order parametric resonance. It is not present for $b < 0.04$ but it emerges suddenly at $b \approx 0.045$ and strongly increases with b. The maximum of the peak is only determined by the nonlinearity in the equation of motion and not by γ. The insets of Fig. 1 show bistabilities leading to hysteresis. If we increase b these hystereses will become more pronounced. Also more higher-harmonic peaks will be visible and higher-order parametric resonances emerge. Above $b \approx 0.85$ the oscillations become chaotic for some values of v. Fig. 2 shows an example of chaotic motion. There is also bistability between chaotic and regular oscillations.

In order to observe all these phenomena in an actual experiment it is necessary that the surface be perfectly periodic along the scan direction over a number corrugation periodicities being much larger (by a factor of 10 say) than the quality factor $1/\gamma$.

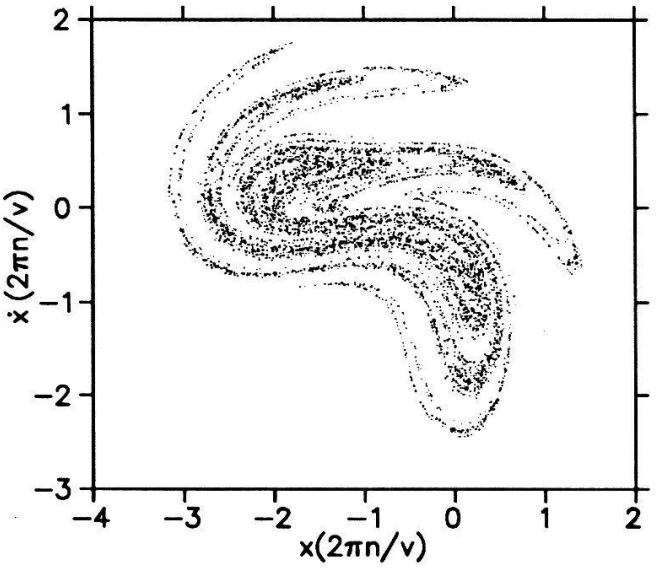

Figure 2: The chaotic attractor for $b = 0.9$, $\gamma = 0.02$, and $v = 1.2$. The points are 5500 snapshots of the system at times which are an integer multiple of $2\pi/v$ (stroboscopic map).

References

[1] G. Binnig, C.F. Quate and Ch. Gerber, Phys. Rev. Lett. **56**, 930 (1986).

Surface Melting of Gallium Single Crystals

Ch. Grütter, R. Trittibach and J.H. Bilgram
Laboratorium für Festkörperphysik, ETH, CH 8093 Zürich

Ellipsometry is used to characterize surfaces of Ga single crystals at temperatures close to the melting temperature T_m. A quasi liquid layer is found at the Ga(112) surface at temperatures below T_m. The optical properties of the layer are inbetween those of the melt and the crystal. The thickness of the layer increases with increasing temperature. This increase can be described by a logarithmic temperature dependence at low temperatures. The correlation length has been determined to ξ = (0.8±0.2)nm. At high temperatures the thickness increases by a power law with power -1/3. The Hamaker constant is W = (4.8±2.0)×10^{-18}mJ. The crossover thickness is comparable with the correlation length.

The Ga(112), Ga(010) and Ga(111) surfaces formig facets on crystals grown from the melt have been investigated. The crystals have been grown at UHV-conditions and the surfaces have been characterizend *in situ* by means of ellipsometry. The structure of the Ga(112) surface ist characterized by a low density of Ga_2-dimers. Referring to general predictions of surface melting, the Ga(112) surface should be a candidate to show a structural transition or thermally induced disordering close to the bulk melting temperature T_m.

The experimentally measured quantities are the ellipsometric angles Ψ and Δ. From these data the optical constants n and k of Ga-crystals at room temperature have been deduced. Approaching T_m changes in the measured data are observed. In fig.1 n and k as measured at the Ga(112) surface along the [$\bar{1}\,\bar{1}$1] direction are plotted vs. temperature.

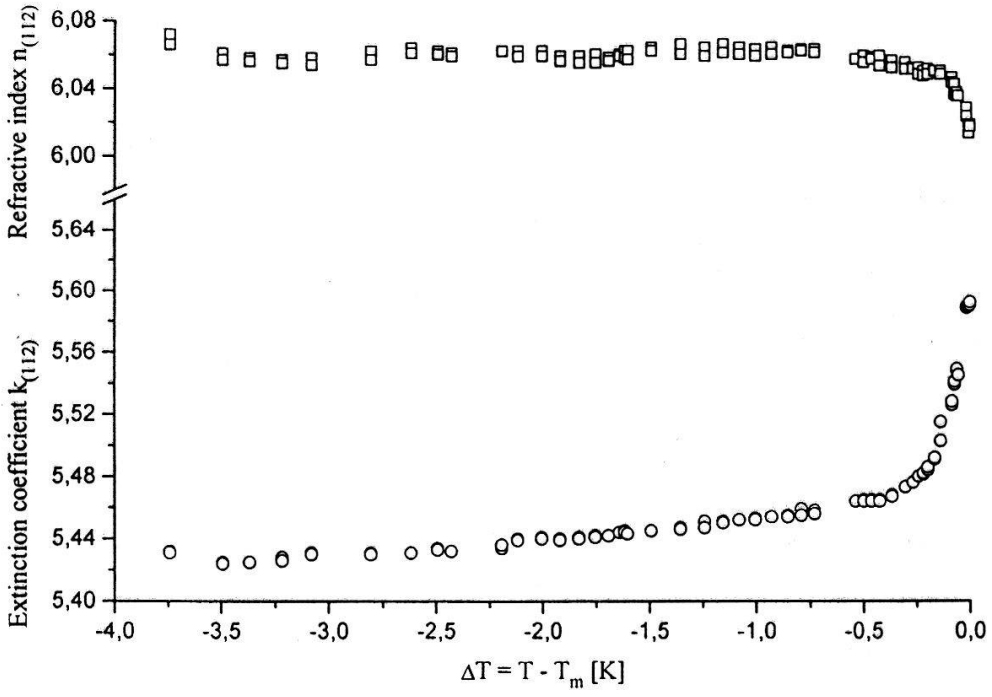

Fig. 1.
Refractive index n and extinction coefficient k as measured at the Ga(112) surface along the [$\bar{1}\,\bar{1}$1] direction vs. temperature.

There are good reasons (e.g. STM studies [1]) to assume that these changes are due to the formation of a quasi-liquid layer at the Ga(112) surface. To deduce the optical properties of this layer we use a simple model of an isotropic substrate covered by a homogeneous, isotropic layer and calculate Δ and Ψ as a function of the increasing layer thickness l^*. For the optical constants of the layer we find the refractive index n=5.80±0.10 and the extinction coefficient k=5.65±0.05, which are close to the optical properties of the crystal bulk. Using these data it is possible to determine the temperature dependence of the layer thickness. We compare the measured variation in ellipsometric angles Δ and Ψ, with a family of curves; once for a logarithmic growth of the layer, as expected if short range forces are limiting the growth of the layer, and once for a power law growth of the layer, as it is expected for the case that long range forces between the interface s-l and l-v limit the growth of the layer. In the temperature range $0.5K<T_m-T<3.5K$ the increase in layer thickness can be described by a logarithmic growth with a correlation length $\xi=(0.8\pm0.2)$nm. In the temperature range $0K<T_m-T<0.2K$ the increase in layer thickness can be described by a power law growth with a Hamaker constant $W=(4.8\pm2.0)\times10^{-18}$mJ. There is a cross-over from a logarithmic to a power law growth at $0.2K<T_m-T<0.5K$ (see fig. 3). The thickness where cross-over occurs ($l_c^*=(0.7\pm0.1)$nm) is comparable with the correlation length within the disordered or quasi-liquid layer, as predicted from theory.

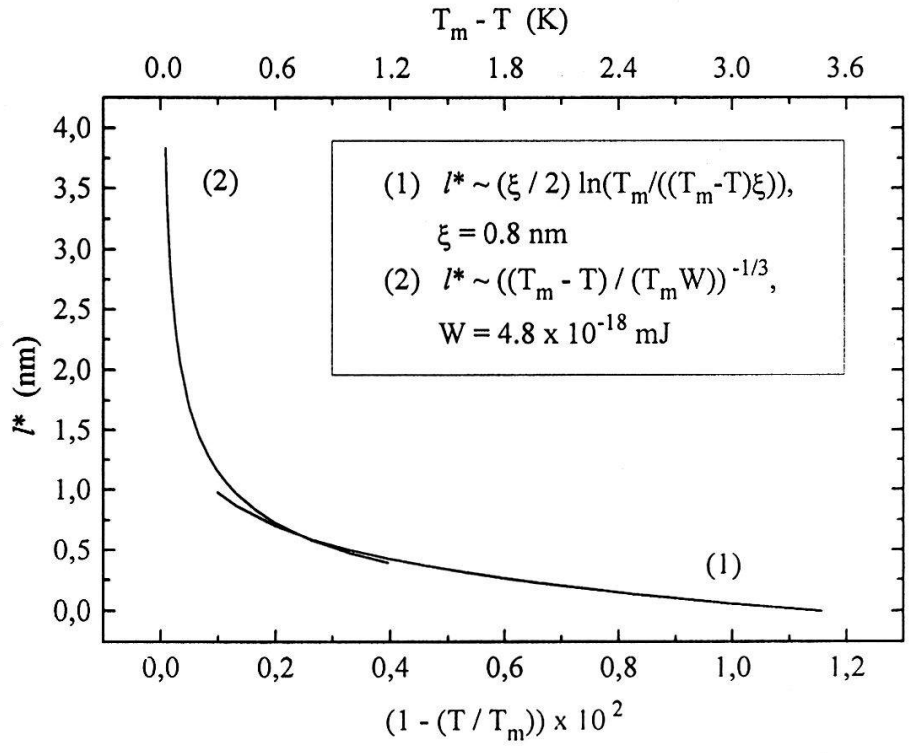

Fig. 3. Layer thickness vs. $1-T/T_m$. The increase in thickness is determined by a logarithmic growth for $T_m-T>0.5K$ with a correlation length $\xi=0.8$nm and by a power law growth for $T_m-T<0.2K$ with a Hamaker constant $W=4.8\times10^{-18}$mJ. The cross-over thickness is comparable with the correlation length in the layer: $l_c^*=(0.7\pm0.1)$nm.

Acknowledgements: We thank Prof. H.R. Ott for his support. This work is supported by the Swiss National Science Foundation.

[1] U. Dürig, Private communication.

COAXIAL PLASMA GUN IN THE HIGH DENSITY REGIME AND INJECTION INTO A HELICAL FIELD

SAMUEL F. SCHAER*)

Centre de Recherches en Physique des Plasmas, Ecole Polytechnique Fédérale de Lausanne, 21 Av. des Bains, CH - 1007 Lausanne, Switzerland

*)*Secondary School Student at:* Gymnasium, Kantonsschule Hardwald, CH - 4600 Olten, Switzerland

ABSTRACT: A modified CPG in the high density regime of 20-70mT of He was investigated. The injection of the plasmatorus into a driftspace was studied by diamagnetical diagnostics both with and without helical bias, where the inner electrode was continued into the driftspace by a central conductor. Quasi-tokamak geometry is obtained ($q\approx3; l_i\approx1.2; \beta_p\approx.7$). Mean speed of torus in driftspace: 2.2cm/μsec; which is in very good agreement with the MHD model derived. Discussion of: (1) general phenomena, (2) second half-period breakdown with autopreionisation, (3) prevention of transv. expansion by rarefaction waves of Mach 50 supersonic flow, (4) stability and homogeneity enhancement, (5) agreement with model, (6) X-points & breakdown dependence. The findings are important for future designs of injectors for magn. confinement.

1. INTRODUCTION

CPG and MAST devices have a wide field of applications in plasma physics. Besides being interesting for fundamental MHD or kinetic theory research, they serve as unique tools for a whole variety of application domains. They are used to fill all kinds of magnetic confinement devices, such as octupoles, tokamaks, mainly for spheromaks with further applications in: space propulsion, dense plasma foci, supersonic flow, plasma centrifuges, etc. . A lot of research on this subject was carried out in the 60ties, but still many questions remained unanswered, so that it is still a research task today, especially if the gun is operated in the high density regime. This work is described in detail in ref. [1].

2. THEORETICAL CONSIDERATIONS

The model that one has to apply is heavily dependent on the particular design characteristics. For each phase of gun operation, i.e. acceleration, ejection, injection, and drift, a different approach has to be pursued. For space reasons, only the acceleration part is described here. For more details, the reader is referred to [1]. The classical snowplow model of Rosenbluth is very well applicable, since :(1) collisions are important, (2) sheet speed < thermal speed, (3) preionisation. Azimuthal exchange is fast because: (1) thermal speed < Alfvén speed, (2) clean breakdown due to second half-period ignition. Wall friction occurs at much higher speeds than encountered in this experiment. Maxwellian electron distribution with T_e=10eV is assumed, which was confirmed by prior investigators using magnetoacoustic oscillation techniques. This is well below the ocurrence of run-away electrons. The snowplowing is both caused by Coulomb turbulence and collisions. The expression for the preceding shock wave and the snowplowed mass is obtained from the Hugoniot-Rankine relations. The capacitor discharge current is assumed sinusoidally, since $t_{ejection}<T/2$. Furthermore, a linear ∇I_{axial} is assumed. A set of two differential equations is then derived choosing rings as infinitesimal elements. Correction factors $\sin\alpha$ and $\cos\alpha$ have to be introduced due to $\nabla u_{z,radial}$. The set is numerically integrated, thus mean values for the correction factors are obtained. It was seen that diffusion can be taken constant for the duration of the experiment; the diffusion coefficient is computed according to the Spitzer relations. It was found that dr/dt only affects the internal density gradient, but not the front surface structure. Upon making these assumptions, the remaining equation is easily solved by variable separation. The analytical solutions have a relative error of less than 2% compared to the numerical integration. They are:

$$z = f\left(-\langle d\rangle + \sqrt{\langle d\rangle^2 + \frac{KI_0^2}{2f\omega^2}(\omega^2t^2-\sin^2\omega t)}\right)$$

$$u_z = \frac{KI_0^2(\omega t - \sin\omega t\cos\omega t)}{2\omega\sqrt{\langle d\rangle^2 + \frac{KI_0^2}{2f\omega^2}(\omega^2t^2-\sin^2\omega t)}} \qquad \text{, where } K = \frac{\mu_0\cos\alpha}{8\pi^2r^2(1+f)\rho_0}$$

<d> stands for the constant diffusion length. The consideration also included the following: current induction in the plasma torus by flux conservation, motion in the drift space, and the computation of the axial equilibrium field according to tokamak geometry. For space reasons, these cannot be discussed here. They are described in detail under [1]. The above formulae also include the velocity limitation

encountered by previous investigators. u_z reaches a plateau after 3 μsec - thus velocity limitation in this experiment is indeed due to snowplowing.

3. EXPERIMENTAL APPARATUS

The CPG used has a length of 15cm and the electrode radii 3 and 5cm. The inner electrode is negative to begin with. A thin, insulated central conductor has been added through the 50cm long driftspace, connected to the inner electrode, for ejection voltage spike suppression and generation of the toroidal bias. It is energized by a capacitor discharge (10-15kV; I up to 86kA), fired by an ignitron controlled by a time base unit with two subsequent amplifier stages including a thyratron pulser. For the connection, a special low inductivity slab line was designed. The axial bias (max. .26T) is generated by a special coil, powered by an aperiodically damped, electrolytic flywheel discharge, which can be timed as the other. For the pressure range of 20-70mT He, a common rotary pump is adequate. In order to reduce oil steam, a liquid nitrogen cryotrap has been added. Otherwise the insulators would quickly become too dirty. All diagnostics are based on magnetical and diamagnetical probe arrays and Rogowski belts. The signals are filtered, then directly fed into DSOs.

4. RESULTS

The CPG was both operated with toroidal and helical bias. The parameters varied are: gas pressure, discharge potential, and the axial bias strength. The optimum parametrs within the investigated variation are: toroidal bias (50mT; 13kV) / helical bias (50mT; 13kV; 0.065T), respectively. 50mT can be predicted to be the optimum pressure for this gun, using our model. With 13kV, the discharge current was 86kA, which is easily predicted using a Laplace network analysis technique. These data were confirmed by the experiment. The current in the torus was 6.4kA, decaying rapidly, but continuously. No n type or oscillatory instabilities occurred. With that, it is found: $q \approx 3$, $l_i \approx 1.2$, $\beta \approx .7$, immediately after ejection. The stability (longer lifetimes, no abrupt instab.) was enhanced by: (1) prevention of transverse expansion by an intercepting rarefaction wave pattern due to the Mach 50 supersonic flow passing between the edges of the muzzle, (2) axial equilibrium field computed according to Shafranov, (3) plasma current decay leading to higher q values. No transverse oscillations were measured at ejection. The prediction of position and speed according to the MHD model is in excellent agreement with time delay measurements. A detailed discussion is found in [1]. The mean speed in the driftspace was 2.2cm/μsec with $t_{ejection}=5\mu sec$, furthermore, the pressure and discharge current dependence were confirmed. The polarity of the inner electrode was chosen negative to begin with, but due to a specific electron deflection effect, the energy of the first half-period is dissipated into preionisation. This has the advantage that breakdown on the second half-period is very clean and homogenous. The shots were absolutely reproducible, vanishing noise levels making up the difference. Therefore, electrode polarity was not changed. Breakdown in the relatively short gun is very sensitive to axial field components. The polarity of the axial bias is such as to confine the ring. A Lorentz force is exerted, so that the plasma current is reversed after a short time. When the field polarity is changed in order to achieve so-called flux-amplification, breakdown occurred at the muzzle (where in this case an X-point with stable electron orbits appears), not allowing proper operation. The axial field coil actually consists of two individual coils, a long and a very short one (which was added after preliminary tests), in order to compensate axial field components in the region of the muzzle. The obvious similarity to Brillouin clouds in magnetrons (cylindrical symmetry) is pointed out. The preceding shock wave with sufficient energy for partial ionisation was measured indirectly, since at ejection, it caused a helical field discharge in the driftspace.

5. CONCLUSION

These findings are of interest to future designs for injection devices for magnetic confinement, especially for spheromaks, where the plasma is produced by two CPGs directed against each other, and of course to CPG research itself. The model derived is in very good agreement with experiment. The performance of the gun was improved (i.e. stability enhancement), the central conductor proved to be rather useful in many ways; autopreionisation just to name one.

6. ACKNOWLEDGMENTS

I thank my mentor Dr.R.Keller, without him, this work would never have existed. I also thank CRPP for their support. The project was financed by ATEL Inc./ Olten.

7. REFERENCES

[1] S.F. Schaer; {*same title*}; CRPP/ LRP 491/94, Feb. 1994 → compl. list of refs. (38)

Improvement of crystal quality of epitaxial silicon-germanium alloy layers by carbon additions

J. Mi, P. Letourneau, J.-D. Ganière, M. Gailhanou, and M. Dutoit
C. Dubois*, J. C. Dupuy*, and G. Brémond*

Institut de Micro- et Optoélectronique, EPFL, 1015 Lausanne, Switzerland
*Laboratoire de Physique de la Matière, INSA, 69621 Villeurbanne, France

Improved $Si_{1-x}Ge_x$/Si hetero-epitaxy has been achieved by RTCVD in the presence of small amounts of C_3H_8 during growth. Carbon presumably scavenges oxygen and acts as a surfactant to inhibit three dimensional growth.

$Si_{1-x}Ge_x$/Si heterostructures have demonstrated significant leverage in silicon technology. However, commensurate epitaxial growth of SiGe layers is accompanied by a built-in strain energy which increases with layer thickness. The system tends to minimize its energy by undergoing strain relaxation through the formation of misfit dislocations and/or islands.

It was reported that the quality of SiGe layers can be improved by the introduction of a surfactant [1] that changes the growth mode from 3 to 2-dimensional growth, and the incorporation of carbon atoms based on the effect of strain compensation [2]. The latter also provides additional flexibility for band-gap engineering. The incorporation of C, however, presents difficult challenges due to the high mismatch between the C and Si lattices, low solubility of carbon in Si and carbide precipitation. C can be kinetically stabilized in substitutional sites in the SiGe lattice by molecular beam epitaxy (MBE) in a well-defined growth regime [3]. Solid phase epitaxy (SPE) is known to allow the incorporation of foreign elements into Si at concentrations far in excess of their solid solubility [4].

Rapid thermal chemical vapor deposition (RTCVD) is compatible with silicon technology. It minimizes the thermal budget and is capable of precise control of surface reactions, which are fundamental for growing thin commensurate layers. It may thus be the ideal technique for producing device-quality SiGeC layers.

SiGe layers were grown on 4-in. n-type Si (100) substrates in a RTCVD system (Jipelec, Jetlight 200). In order to minimize the adsorption of water vapor on the surface, wafer loading and unloading were carried out within 40 second during which the temperature of the chamber walls was kept at about 40°C. The partial pressure of water vapor was monitored by a mass spectrometer and was below 10^{-5} torr during growth. Before epitaxy, an *in situ* hydrogen bake at 1100 °C was performed. The samples reported here were grown at 900°C and 1 torr. Hydrogen was used as a carrier gas (1000 sccm). Pure SiH_4 and a mixture of 1% GeH_4 in hydrogen served to grow SiGe layers. GeH_4 flow rates were varied resulting in different Ge contents up to 10 at. % and thicknesses of 130 to 170 nm. These values are close to the critical thickness. A mixture of 1% C_3H_8 in hydrogen was added during the growth. The growth rate decreased with increasing C_3H_8 flux. The layers were characterized by x-ray diffraction (XRD), photoluminescence (PL) spectroscopy, secondary-ion mass spectrometry (SIMS) and transmission electron microscopy (TEM).

No disruption of the epitaxy due to C additions is observed (Fig. 1). Instead, the SiGe quality is greatly improved by C_3H_8. The pendellosung fringes for the SiGe alloy in the (113) XRD rocking curves (Fig.1 b) are indicative of a sharp interface and good crystalline quality. The PL spectra provide evidence for the disappearance of dislocation peaks (D_1, D_2 and D_4) and a red shift of the excitonic NP line for films grown with C_3H_8 (Fig. 2). The latter indicates that the layers grown with C were less relaxed. SIMS analysis indicates that little, if any C atoms were incorporated into the film and therefore there is probably no strain compensation.

At 900°C, the growth is controlled by the adsorption of Ge and the growth front is free of hydrogen. C_3H_8 is easily decomposed at 900°C [5]. During growth, C atoms tend to compete with Si and Ge atoms for available sites on the surface. They influence the adsorption of Si and Ge atoms and reduce their mobility. C atoms can also react with oxygen in the chamber. It is more

likely however that C present on the growth front acts as a surfactant and facilitates 2-dimensional growth, which results in improved crystal quality.

In summary, RTCVD-grown SiGe crystallline quality can be improved in the presence of very small amounts of C_3H_8. This can be explained by the scavenging of residual oxygen in the chamber and the surfactant effect of C atoms during growth. Due to the fact that the sticking coefficients of C species are very low, it is not likely that under the conditions used in this work, strain compensation is playing a role.

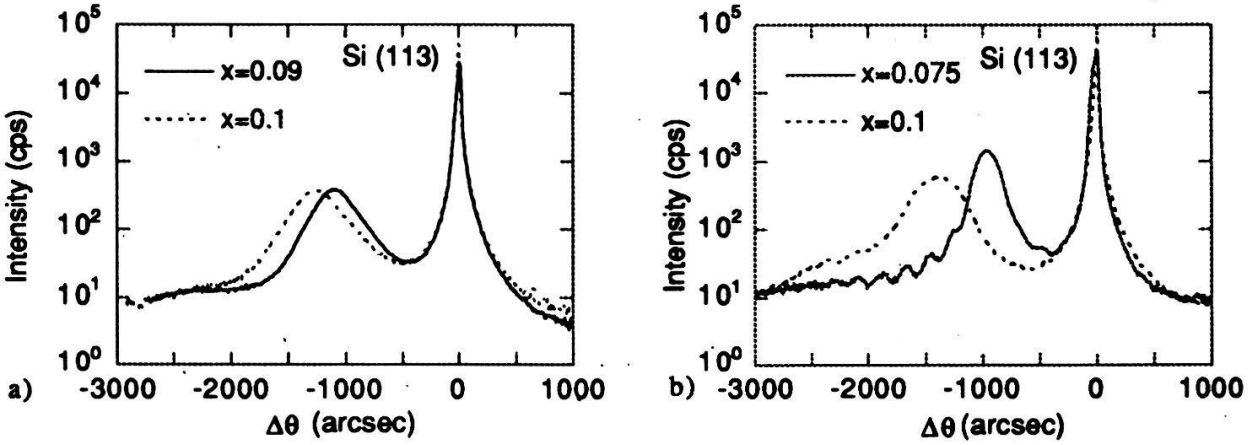

Fig. 1 XRD Spectra for $Si_{1-x}Ge_x/Si$ structures grown without (a) and with (b) C_3H_8 flux.

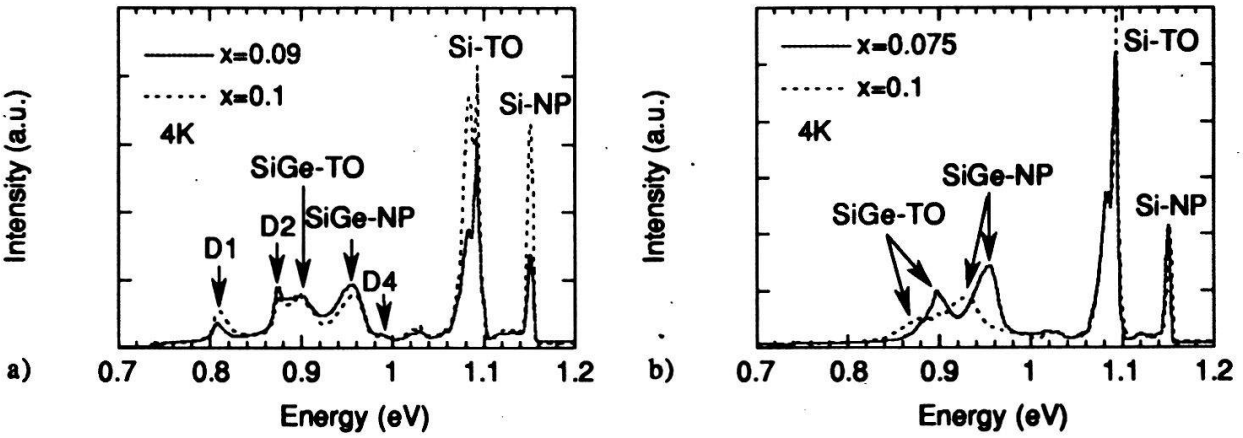

Fig. 2 PL Spectra for $Si_{1-x}Ge_x/Si$ structures grown without (a) and with (b) C_3H_8 flux.

References

[1] M. Copel, M. C. Reuter, E. Kaxiras and R. M. Tromp, Phys. Rev. Lett. 63, 632 (1989)
[2] S. Im, J. Washburn, R. Gronsky, N. W. Cheung and K. M. Yu, Appl. Phys. Lett. 63, 929 (1993)
[3] K. Eberl, S. S. Iyer, S. Zollner, J. C. Tsang and F. K. LeGoues, Appl. Phys. Lett. 60, 3033 (1992)
[4] J. W. Strane, H. J. Stein, S. R.Lee, B. L. Doyle, S. T. Picraux and J. W. Mayer, Appl. Phys. Lett. 63, 2786 (1993)
[5] C. D. Stinespring and J. C. Wormhoudt, J. Appl. Phys. 65, 173 (1989)

Individual Holographic Optical Element for Output-Emission Improvement of a Diode-Laser Array

R. Spring, W. Lüthy and H.P. Weber
Institute of Applied Physics, University of Bern, Sidlerstrasse 5, CH - 3012 Bern, Switzerland

An individual Holographic Optical Element (HOE) for a diode-laser array is recorded using the 813 nm diode output emission itself. The HOE transforms the emission pattern of the diode-laser array into that of a diffraction limited single stripe emitter. The feasibility of this method is demonstrated.

Diode lasers as pump sources have obtained an increasing importance due to their high efficiency, reliability, compactness and simplicity in handling. A single-stripe laser diode emits a cone of coherent light with a power up to about 150 mW. In order to get more power several emitters are arranged in an array as e.g. in the cw 1 Watt diode-laser array "Siemens SFH 480401". This array consists of 20 individual phase-coupled emitters with a total dimension of 200 μm horizontally and 1 μm vertically. Each single emitter radiates coherent light at a wavelength of 813 nm with a phase-shift of π with respect to adjacent emitters. The emission output thus becomes a dual-lobed ellipical pattern with vertical divergence of 39° FWHM and a horizontal divergence of 13° FWHM [cf Fig. 1]. Therefore an optical system with a sufficiently large numerical aperture is needed for collimating and focusing the highly divergent diode-laser light emission into the laser crystal. In order to pump efficiently, a good overlap of pump light and laser mode is required. Possible solutions for optical coupling make use of microlenses, fiberoptic pigtails or monolithically integrated elements. All these coupling methods suffer from a variety of drawbacks, notably expense, complexity and difficulty in scaling. A Holographic Optical Element (HOE), however, can transform the diode-laser emission into a desirable optical output. Unfortunately as yet there are no photographic materials available with very high spatial resolution (> 4000 line pairs per mm) and sufficient sensitivity (exposure times < 1 s) in the IR-wavelength range. Nevertheless higher exposure times and sufficient mechanical stability of the setup allow recording of a HOE. Recently there has been progress in recording holographic patterns in the deep red but the spectral range above 750 nm has not been opened up to now. There is a possible solution in order to get a feasible HOE in the IR wavelength range above 750 nm by recording the hologram with a visible wavelength and by illuminating it with IR light. Another possible solution is to calculate the desired interference pattern with the help of a computer and to realize it with photolithographical techniques. Computer generated HOEs promise quite high diffraction efficiencies of up to 70 %. With this method, however, the fine and individually characteristic structure of each diode-laser emitter is lost. We report on the feasibility of the recording process of an individual amplitude hologram with the 813 nm diode output emission itself. Since the diffraction efficiency for amplitude holograms is theoretically restricted to 6.25 % no effort is made to enhance the diffraction efficiency to an optimum value. A thick phase HOE with the same recording process promises a maximum theoretical dif-

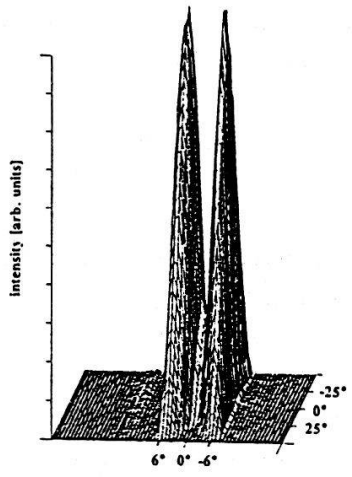

Fig. 1 : Far-field intensity pattern of diode-laser emission

fraction efficiency up to 100 %. For recording a HOE, the path difference between reference and object beam must be smaller than the coherence length of the light source. Since the diode laser array used in our experiments has a bandwidth of about 2 nm (≈ 1 THz), the coherence length is only 0.3 mm, thus requiring small tolerances in path length difference. For this reason an optical set-up using a Mach-Zehnder interferometer with a total path length of 47 cm was chosen as shown in Fig. 2. To obtain sufficient vibration and temperature stability, the laser and the entire optical set-up were mounted on a vibration isolated pneumatic table and covered with a metallic housing to avoid air turbulence while recording. The output emission of the laser diode array (D) passing the optical shutter (Sh) is imaged with a microscope lens system (L) onto the image planes located at the slit (S) and the plane (S') respectively. The distance between (D) and (L) is adjusted to get a magnification of 25. The divergence of the diode-laser array output is reduced by (L) to 1.56° x 0.52° FWHM according to the chosen magnification. Using a beam-splitter (B) the emission of the diode array is split into a reference beam (R) and an object beam (O). While (R) is not filtered at (S'), (O) is limited by the slit (S), transmitting ideally just the magnified image of one single stripe. (S) reduces the light intensity of (O) by a factor of 20. Therefore, two neutral density filters (N) with a total transmitting factor of 0.045 are introduced in (R) to balance the intensities of (O) and (R). The HOE created by the superposition of (R) and (O) can reconstruct a single stripe upon illumination with the whole diode-laser array. For recording the HOE the emulsion of Agfa-Gevaert "Holotest 8 E 75 HD NAH" was used. It exhibits a grain-size of approximately 35 nm and has a very high theoretical resolving power of 5000 lines/mm. The emulsion is sensitised for 600 nm up to 750 nm. For longer wavelengths the sensibility of the emulsion decreases rapidly. Due to the recording wavelength of 813 nm, high recording light intensities and long exposure times are required. Therefore an exposure time in the range between 30 s and 60 s was chosen for recording the hologram. After recording the HOE was processed with Agfa-Gevaert "GP61" developer. For reconstruction, the HOE was put back into the film holder in the same position as for recording. Illumination of the HOE with the whole diode-laser emission (R) and blocking the object beam (O) reproduces the single lobed image of a single stripe emitter. The result of the reconstructed object beam is analyzed with the help of a ccd-camera and shown in Fig. 3. The single lobe shows a horizontal divergence of 1.56° FWHM and a vertical divergence of 0.06° FWHM, ten times smaller than the corresponding divergence angle of the reference beam. In **conclusion** we have shown that a HOE can be recorded with the 813 nm diode-laser light itself. With such a HOE it is possible to colliminate the diode output. We have demonstrated the transformation of the dual-lobed emission of a diode-laser array into the diffraction limited single lobed emission of a single laser stripe.

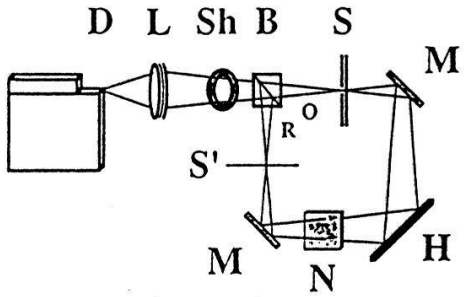

Fig. 2 : Experimental arrangement with : Diode-laser array (D); Lens (L); Optical shutter (Sh); Beam splitter (B); Slit (S); Image plane (S'); Mirrors (M), Neutral density filters (N); HOE (H)

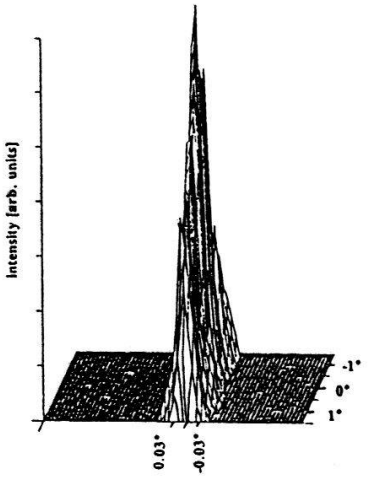

Fig. 3 : Reconstructed far-field intensity pattern of a single stripe

Abbildung einer stehenden evaneszenten Welle mit optischer Nahfeld-Mikroskopie

M. A. Bopp, G. Tarrach, A. J. Meixner, und I. Zschokke-Gränacher

Institut für Physik, Universität Basel, Klingelbergstrasse 82, CH-4056 Basel

We present the analysis of a standing evanescent wave which is caused by total internal reflection of an Ar-ion laser beam on a glass prism, and investigate the coupling to a sub-wavelength dielectric tip of a scanning near-field optical microscope (SNOM) which is raster scanned at close distance over the prism surface. The intensity of the evanescent field is spatially modulated with a period of 239.2 nm. It decays exponentially with a constant of 103.9 nm with increasing distance from the prism surface. Precise measurements of the standing evanescent wave allow to determine the spatial resolution to better than 160 nm and the coupling efficiency of the tip to 63%.

Im optischen Raster-Nahfeldmikroskop (SNOM) werden die Vorteile der klassischen Lichtmikroskopie, nämlich die Wellenlängen- und Polarisationssensitivität, mit der hohen Auflösung der Raster-Sonden-Mikroskopie (STM, AFM) kombiniert. In der klassischen Optik ist die Auflösung durch die Beugung auf die halbe Wellenlänge des verwendeten Lichtes begrenzt. Die Idee, wie man diese Beugungsgrenze umgehen könnte stammt von Synge [1]. Er schlug vor, an einem dünnen, lichtundurchlässigen Schirm eine Öffnung mit einem Durchmesser der deutlich kleiner ist als die halbe Lichtwellenlänge anzubringen. Bei Bestrahlung dieses Schirmes mit einer intensiven Lichtquelle sollte es einigen Photonen gelingen durch die Öffnung zu tunneln. In der Nähe dieser Öffnung (wieder im Abstand kleiner als die halbe Lichtwellenlänge) ist daher das elektrische Feld sehr stark lokalisiert. Man erhält so eine Punktlichtquelle, welche nicht durch die Beugung begrenzt ist. Gelingt es, diesen Lichtpunkt in einem Abstand kleiner als die halbe Lichtwellenlänge über die Probe zu rastern und das transmittierte Licht zu detektieren, dann hat man ein optisches Raster-Nahfeld-Mikroskop realisiert. Diese Idee konnte aber aus technischen Gründen erst vor 10 Jahren durch Pohl [2] und Lewis [3] verwirklicht werden.

Heute verwendet man als Schirm üblicherweise eine ausgezogene Glasfaser. Wir können sie mit einer selbstgebauten Apparatur in einem kombinierten Zug- und Heizprozess zu einer feinen Spitze von 100 - 200 nm Durchmesser ausziehen. Die Spitze kann sowohl als Lichtquelle, wie auch als Detektor, welcher das optische Nahfeld unserer Probe detektiert, eingesetzt werden.

Diesen zweiten Fall haben wir für unsere Experimente angewendet. Mit der aus der Raster-Sonden-Mikroskopie bekannten Piezotechnik kann die Spitze in kontrollierter Weise in geringem Abstand über die Probe gerastert werden. Das in die Spitze eingekoppelte Licht wird durch die Glasfaser zum Detektor, einem Photomultiplier, geleitet (Figur 1). Als abzubildende Struktur verwenden wir die Intensitätsmodulation einer stehenden evaneszenten Welle. Diese Welle bildet sich aus der Überlagerung zweier sich entgegenlaufender evaneszenter Felder, welche bei der Totalreflexion eines Laserstrahles (in unserem Fall ein Ar-Ionenlaser bei 514.5 nm) an einer Prismenoberfläche entstehen.

In Figur 2 ist eine Messung auf einer sauberen Prismenoberfläche gezeigt. Die Spitze wurde in konstanter Höhe in x-Richtung über das Prisma gerastert. Nach jeder Linie wurde der Abstand zur Oberfläche etwas verringert und die gleiche Linie wieder aufgenommen. Dieser Abstand ist in Figur 2 in der z-Achse aufgetragen. Die P-Achse schliesslich beschreibt die vom Detektor gemessene Lichtleistung.

Aus Figur 2 ergibt sich für die stehende Welle eine Periode von 239.2 nm. Dieser Wert lässt sich auch aus der Wellenlänge des Laserstrahles, dem Einfallswinkel θ und der Brechzahl des Prismas exakt berechnen. Man kann dadurch also die laterale Auslenkung des Piezoscanners eichen. Aus der gemessenen Modulationstiefe der stehenden Welle lässt sich die effektive Einkopplungsfläche der Spitze bestimmen. Die Einkopplungscharakteristik wird dazu durch eine rotationssymmetrische Gauss-Funktion modelliert. Durch einen Vergleich mit der Messung erhält man einen effektiven Einkopplungsradius der Spitze von 80 nm. Dieser Wert stimmt sehr gut mit der durch Elektronenmikroskopie bestimmten Spitzengeometrie überein. Die laterale Auflösung unseres Nahfeldmikroskopes beträgt also mindestens 160 nm, was mit keinem klassischen optischen Mikroskop erreicht werden kann.

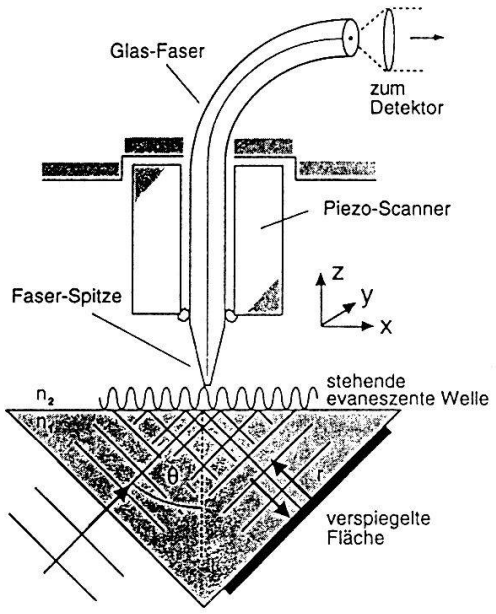

FIG. 1. Aufbau des Nahfeldmikroskopes zur Abbildung der stehenden evaneszenten Welle

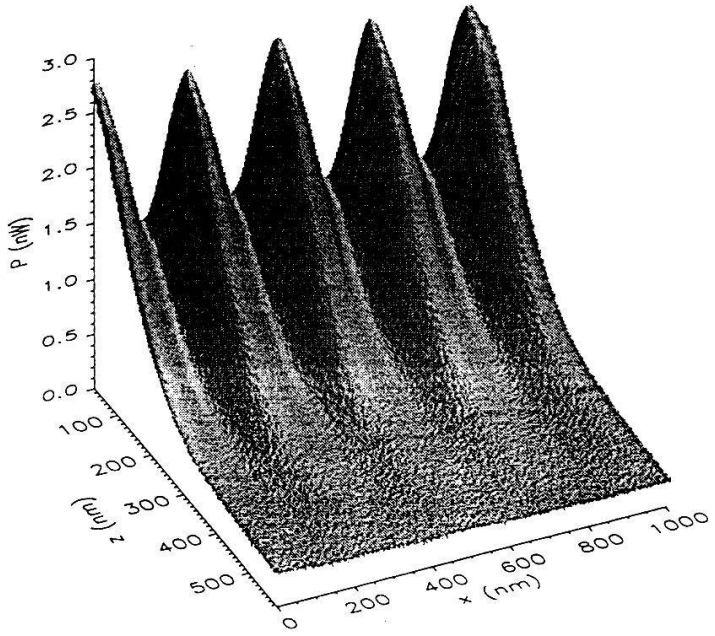

FIG. 2. Räumliche Modulation der stehenden evaneszenten Welle (x-Richtung), exponentieller Zerfall der Intensität mit wachsendem Abstand der Spitze von der Oberfläche (z-Richtung) und die vom Detektor gemessene Lichtleistung (Ordinate)

Bei der Annäherung der Spitze an das Prisma ist zu erkennen, dass das evaneszente Feld exponentiell ansteigt. Nahe an der Oberfläche flacht dieser Anstieg jedoch ab. Dies ist auf eine Störung des evaneszenten Feldes durch die Glasfaserspitze zurückzuführen. Mit einem Modell, welches die Glasfaser durch ein unendlich ausgedehntes Dielektrikum im Abstand z von der Oberfläche approximiert, lässt sich dieser Verlauf sehr gut beschreiben. Im Weiteren kann damit auch die Einkoppeleffizienz in die Spitze bestimmt werden. Sie beträgt 63%. Dieser hohe Wert ist sehr vielversprechend für spätere Anwendungen zum Beispiel in der Spektroskopie.

Diese Arbeit wurde unterstützt durch das Schwerpunktsprogramm "Optik" des Bundes, den schweizerischen Nationalfonds und den Treubel-Fonds Basel.

[1] E. H. Synge, Philos. Mag. **6**, 356 (1928)
[2] D. W. Pohl, W. Denk, and M. Lanz, Appl. Phys. Lett. **44**, 651 (1984)
[3] A. Lewis, M. Isaacson, A. Harootunian, and M. Muray, Ultramicroscopy **13**, 227 (1984)

Charge dependent freezing line of Yukawa suspensions

T. Palberg, W. Mönch, F. Bitzer, P. Leiderer, L. Belloni#, T. Bellini* and R. Piazza*
Universität Konstanz, Fak. f. Physik, D-78434 Konstanz, Germany
#CEA, Centre d'Etudes de Saclay, Bat 125, F-91191 Gif-sur-Yvette cedex, France
*Universita di Pavia, dip. ellettronica appl. I-27100 Pavia, Italy

We present the freezing line of monodisperse colloidal latex spheres suspended in aqueous electrolyte as function of the number of ionic surface groups and the concentration of screening ions. Experimental data are quantitatively described using the results from recent computer simulations, if the coupling between dissociation equilibrium and counter ion condensation is taken into account.

Charged colloidal suspensions are considered as model Yukawa fluids which are easyly acessible by optical methods. The transformation of the experimental variables into Yukawa potential parameters [1] was recently tested at constant particle charge [2]. Variation of charge so far was confined to micellar systems with low number of ionic groups N. We here use FEP latices carrying $N=10^2-10^3$ physisorbed ionizable groups. The number of actually dissociated charges Z(N) is smaller than N ($pk\approx4$). Yukawa parameters are calculated via charge renormalization procedures [3] yielding an effective charge $Z_{PBC}\leq Z$. Also an effectively transported charge $Z^*(\sigma)$ is derived from the conductivity σ.
The particle density of $\rho=6.31\ 10^{19}\,m^{-3}$ and μmolar salt concentrations c_S are adjusted using advanced deionization techniques [4]. In intense contact to ion exchange resin N and σ are slowly reduced due to desorption. A N/σ calibration curve was recorded via conductimetric titration with NaOH.
The coexstence region plotted in Fig.1 as vertical bars was

determined by microscopic observation under stepwise lowering of N and subsequent addition of salt. It separates the fluid phase from the bcc crywstalline phase It is compared to theoretical predictions of the freezing line for five different charge numbers used as input [2]. Using N (-·-·-), Z(N) (·····) or $Z_{PBC}(N)$ (---) grossly overestimates the stability of the solid phase. The calculation of renormalized charges under conditions of constant dissociation equilibrium $Z_{PBC}(Z(N))$ (——) yields a quantitative prediction with the surfactant pk=4.05 as only fit parameter. Note, that the use of $Z^*(\sigma)$ unexpectedly allows for a qualitative prediction (∉) of the phase behaviour from conductivity.

[1] M. O. Robbins, K. Kremer and G. Grest, J. Chem. Phys. **88**, 3286 (1988).

[2] F. Bitzer, T. Palberg, H. Löwen, R. Simon and P. Leiderer, Phys. Rev. E, submitted (1994).

[3] S. Alexander, P. M. Chaikin, P. Grant, G. . Morales, P. Pincus and D. Hone, J. Chem. Phys. **80**, 5776 (1984).

[4] T. Palberg, W. Härtl, U. Wittig, H. Versmold, M. Würth and E. Simnacher J. Phys. Chem. **96**, 8180 (1992).

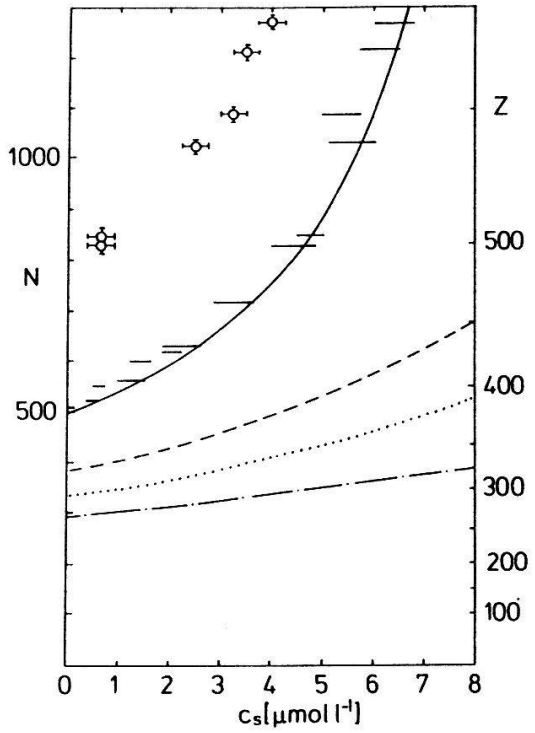

Fig.1: Experimental freezing line (o) as function of N and c_s compared to theoretical predictions. See text for details.

Dynamics of Giant Polymer-like Microemulsions

Carolina Cavaco and Peter Schurtenberger

Institute für Polymere, ETH Zürich, CH-8092 Zürich, Switzerland

We report a study of the dynamic properties of polymer-like lecithin water-in-oil microemulsions using rheological measurements. These systems form a viscoelastic network at concentrations higher than the overlap concentration, Φ^*. The results from the frequency dependent measurements are discussed in terms of possible mechanisms for stress relaxation using recently developed theories for 'equilibrium polymers'. Particular emphasis is given to a critical examination of the possibility of formation of a crosslinked versus an entangled network of polymer-like micelles.

In contrast to classical polymer solutions, where the degree of polymerization is fixed, in micelles and microemulsions, which are formed by weakly interacting monomers, the average aggregation number N depends on surfactant concentration and temperature. Micelles are thus transient structures that can break and recombine offering additional mechanisms for stress relaxation. A theoretical model that describes the dynamic behavior of 'equilibrium polymers' has been developed by Cates [1], [2], [3]. This model is based on the reptation theory [4] and takes into account the equilibrium molecular weight distribution and the finite life time of equilibrium polymers. According to this model, the dynamic properties of viscoelastic surfactant solutions are mainly controlled by two processes: reptation as in classical polymer solutions and breakage and recombination of the micelles. This model predicts a nearly single exponential decay of the stress relaxation in the limit where the micelle breaking time is short when compared to the reptation time [1], [2].

The addition of very small quantities of water to soybean lecithin reverse micellar solutions results in an anisotropic one-dimensional micellar growth and formation of giant polymer-like reverse micelles. At volume fractions $\Phi > \Phi^*$, a transient viscoelastic network is formed with a corresponding strong increase of the zero shear viscosity η_S. We have previously suggested that these systems could be used as good models for an experimental realization of equilibrium polymers. Using results from static and dynamic light scattering [5] and small angle neutron scattering [6] experiments we were able to confirm the cylindrical structure and high flexibility of the micellar aggregates. Light scattering experiments show a strong dependence of the micellar size on the water to lecithin molar ratio w_o: the micellar size increases dramatically with increasing w_o until a plateau is reached. A further increase of w_o does not result in an increase of the micellar size. Concomitantly, the zero shear viscosity increases dramatically with increasing w_o and reaches a distinct maximum at a well defined $w_{o,max}$. Upon further addition of water the zero shear viscosity decreases and phase separation can be observed.

In the semidilute regime these systems exhibit a viscoelastic behavior similar to that observed in semidilute solutions of classical polymers. For viscoelastic solutions of lecithin in cyclohexane the dependence of the zero shear viscosity on the volume fraction can be described by a power law of the form $\eta_S \sim \Phi^x$ with exponents x that appear to be in agreement with the 'equilibrium polymer' model, which predicts an exponent of 3.5 [7].

For lecithin/isooctane solutions at low water content we find $\eta_s \sim \Phi^{3.66}$, in agreement with the model. However, for solutions with higher water content, where giant polymer-like micellar aggregates are formed we have found $\eta_s \sim \Phi^{1.9}$. An exponent of 1.9 is far too low when compared to the value predicted by the 'equilibrium polymer' model. Even the incorporation of faster stress relaxation mechanisms such as breathing and Rouse motion lead to a theoretical exponent of 3.0 only, [7], [8] i.e. it can not account for the exponents found experimentally.

A more sensitive method of evaluating dynamic properties are frequency dependent measurements of the storage modulus $G'(\omega)$ and the loss modulus $G''(\omega)$ for which qualitative predictions exist on the basis of the 'equilibrium polymer' model [9]. For lecithin/isooctane solutions at high water content the representation of $G''(\omega)$ *versus* $G'(\omega)$ in the so-called Cole-Cole plot shows a semicircular shape, indicating the presence of a single relaxation time or a narrow distribution of relaxation times in good agreement with the 'equilibrium polymer' model. While the dynamic measurements agree with the predictions of the 'equilibrium polymer' model, the dependence of η_s on Φ can not be explained by the same model in the limit of very large micellar sizes.

The representation of the frequency dependent shear moduli in Cole-Cole plots for viscoelastic solutions of lecithin in cyclohexane show a strong deviation from the single exponential behavior expected, indicating the presence of a wide distribution of relaxation processes. The formation of a network of interconnected micelles at volume fractions higher than Φ^* could be a possible explanation for this broad distribution of relaxation times. Mechanisms for stress relaxation in a connected network such as the crossability of two micelles or the sliding of crosslinks along the micelles were recently suggested by Appell *et. al.* [10] to explain the rheological behavior of aqueous surfactant solutions of $CPClO_3$.

Preliminary results of lecithin and water long time self diffusion coefficient measurements in lecithin/cyclohexane solutions indeed suggest that the formation of a connected network takes place at lecithin volume fractions higher than the crossover volume fraction, Φ^*.

Acknowledgments

This work was supported in part by the Portuguese National Fund for Technological and Scientific Research through the Grant BD/1256/91-IC.

References

[1] Cates M.E., Macromolecules **20**, 2289 (1987).
[2] Cates M.E., J. Phys. (Paris) **49**, 1593 (1988).
[3] Cates M.E., J. Phys. Chem. **94**, 371 (1990).
[4] Doi, M., Edwards, S.F., The Theory of Polymer Dynamics (Clarendon, Oxford, 1986)
[5] Schurtenberger, P.; Cavaco, C., Langmuir **10**, 100 (1994).
[6] Schurtenberger, P., R. Scartazzini, L.J. Magid, M.E. Leser and P.L. Luisi J. Phys. Chem. **94**, 3695 (1990). Schurtenberger, P., L.J. Magid, S. King and P. Lindner J. Phys. Chem. **95**, 4173 (1991).
[7] Cates M.E. and S.J. Candau, J.Phys.: Condens. Matter **2** , 6869 (1990).
[8] Schurtenberger, P.; Scartazzini, R.; Luisi, P.L., Rheol. Acta **28**, 372 (1989).
[9] Granek, R. and M.E. Cates J. Chem. Phys. **96**, 4758 - 4767 (1992).
[10] Appell J., G. Porte, A. Khatory, F. Kern and S.J. Candau, J. Physique II **2**, 1045 (1992).

360° Panoramic View Isochronous Time-of-Flight Mass Spectrometer

R. Kallenbach, P. Wurz, L. Gubler, M. Gonin and P. Bochsler

Physikalisches Institut, Universität Bern, Sidlerstr. 5, 3012 Bern

Employing a magnetic field to limit the divergence of ion trajectories in isochronous time-of-flight spectrometers can improve the detection efficiency and thereby reduce the background if compared to the already realized instrument CYLMAS. The time-of-flight section can be combined with a toroidal entrance system and sectorized pixel array detectors to yield a 360° field-of-view mass spectrometer. The sectorization of such an instrument to be flown on a spinning spacecraft allows a complete mapping of the velocity distribution of the investigated particles and it leads to a further reduction of the counting background and a significant improvement of the mass resolution.

The concept of the instrument is shown in Fig. 1. An ion with mass M can enter into the time-of-flight section of the spectrometer through a toroidal electrostatic analyzer covering a panoramic view angle of 360°. Passing through a thin carbon foil the ion will release secondary electrons, thereby generating a start puls at the beginning of the flight path. Simultaneously, charge exchange in the foil occurs leading to a significant fraction of singly ionized particles ($Q = 1$) or neutrals ($Q = 0$). At the end of its trajectory through the

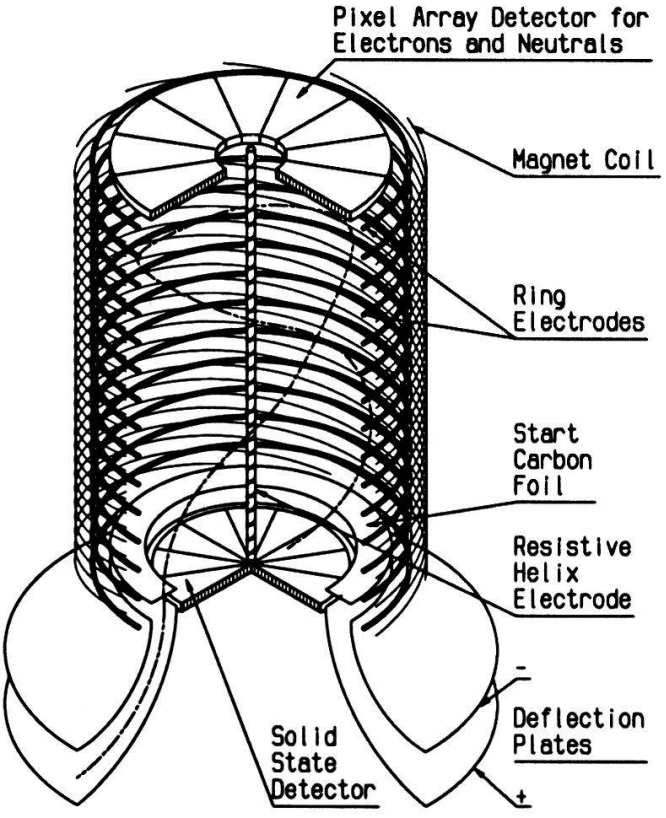

Figure 1: Concept of the instrument

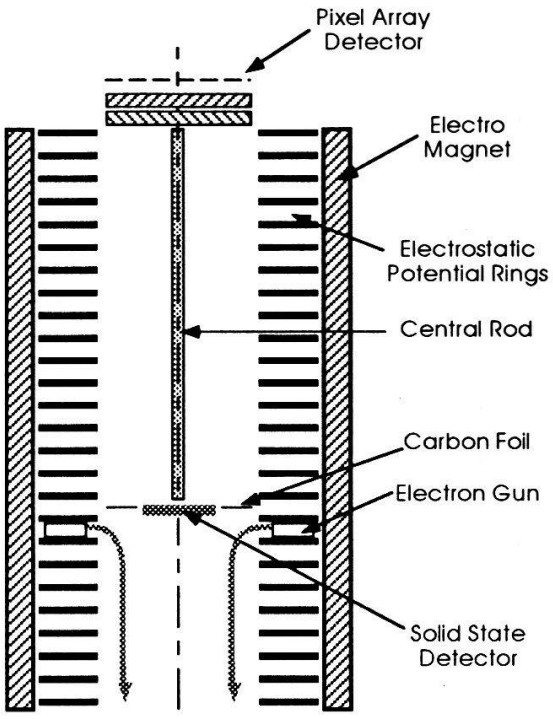

Figure 2: Neutral gas analyzer

isochronous time-of-flight section the ion will hit a solid state detector where its energy is measured. At the same time, secondary electrons released from the solid state detector will trigger a stop signal on the pixel array detector. The electric potential $V(r,z)$ of the time-of-flight section is generated by ring electrodes and a central rod with a resistive helix electrode: $V(r,z) = V_o(2z^2 - r^2)/2z_0^2 - V_1 \ln(r/R)$. As required for an isochronous time-of-flight mass spectrometer the motion in z-direction is a simple harmonic oscillation with frequency ω_z given by $\omega_z^2 = 2V_0Q/Mz_0^2$. The logarithmic potential is attractive towards the central axis and compensates for the radial harmonic term which causes diverging trajectories. The magnetic field increases the angular acceptance of the instrument. Any radial motion will be bound by an axial magnetic field. The equations of motion can be written in reduced units:

$$\frac{d^2\rho}{d\tau^2} = \frac{\gamma(\frac{M}{Q})}{2}\rho - \frac{\delta}{\rho} + \frac{(1-2\beta)^2}{4\rho^3}; \qquad \frac{d^2\zeta}{d\tau^2} = -\gamma(\frac{M}{Q})\zeta$$

In these equations time is measured in units of the inverse angular Larmor frequency $\omega_B = QB_0/M$, and radial distance ρ is measured in units of the radius r_0 of the entrance circle to the axis of symmetry. $\gamma(\frac{M}{Q})$ gives the ratio between ω_z^2 and ω_B^2 and therefore determines the ratio of the electric field of the harmonic potential and the magnetic field strength. The energy range of particles to be analyzed determines the size of the instrument for given field strengths. The parameter δ of the logarithmic potential can be adjusted to obtain an optimum distance range ρ where an ion hits the solid state detector. The parameter β in the centrifugal force term is the initial angular velocity $\dot{\phi}_0$ in units of the Larmor frequency. β is essentially determined by the angular spread of the ion trajectories after their passage through the carbon foil. At sufficiently high magnetic fields, β becomes negligeable. Therefore, we expect to concentrate the particle flux by at least a factor of 10 with the application of a permanent magnetic field. Furthermore, the secondary electrons emitted from the start carbon foil or those from the stop detector can be imaged with high spatial resolution on the pixel array on top of the instrument because they are well focused by the magnetic field. This helps to reduce background signals due to erronous coincidences.

We also consider the application of such an instrument as a neutral gas analyzer, e.g. for the application in cometary atmospheres. In Fig. 2 we show the entrance region with a ring-shaped electron source. The electrons will be guided by the magnetic field and their collision rate with neutral atoms or molecules will be increased by the spiraling motion in the field. Ionized positive particles will be accelerated towards the entrance carbon foil.

With the exception of the magnetic field configuration, all parts of the instrument have been tested in the form of a laboratory prototype [1]. Depending on the application, magnetic fields on the order of 0.1 Tesla to 1.0 Tesla are necessary to significantly improve the performance in comparison to the non-magnetic CYLMAS-instrument. Fields of the order 0.1 Tesla are easily feasible with permanent magnets. Especially, for the analyze of rare isotopic species in the solar wind, field strengths of 1.0 Tesla are preferable. Only superconductors could generate such high fields with a reasonable effort on spaceborne experiments. We hope that superconductors will soon become available for space applications.

References

[1] L. Gubler, "Isochrone Flugzeit-Massenspektrometer für den Einsatz im Weltraum", PhD thesis, University of Bern, 1994.

HYDROGENATION OF CO_2

B. Eliasson and E. Killer
Baldur Eliasson, ABB Corporate Research, Global Climate Change, CH-5405 Baden, Switzerland

A description is given of a method for transforming carbon dioxide, a greenhouse gas, into methanol, a useful fuel.

One of the global environmental problems facing mankind is the threat of global warming of the atmosphere. This so-called man-made greenhouse effect is caused by emissions of certain gases, foremost among them carbon dioxide. Carbon dioxide is generated whenever fossil fuels are combusted. If it ever becomes necessary to limit the emissions of carbon dioxide to the atmosphere large amounts of CO_2 might have to be removed from the flue gases of power plants. This carbon dioxide may have to be recycled or disposed of. One possible recycling mechanism is to use the carbon dioxide as a source of carbon for making hydrocarbons. Methanol is one of the simplest hydrocarbons. It can be used as a fuel or as a source for further hydrocarbon chemistry [1].

In this article we report on hydrogenating carbon dioxide by combing it directly with hydrogen. Today methanol is made from syngas, i.e. a combination of carbon monoxide and hydrogen which is derived directly from natural gas, coal or oil. In our scheme the hydrogen would have to be supplied in a carbon dioxide free way, i.e. by using solar power, hydro power or nuclear power. Hydrogen made in such a way is very expensive today and this method of generating methanol is not competitive with fossil fuel based methanol. In the future, however, the boundary conditions might change. The possibility of a tax on carbon emissions or the much talked of future hydrogen economy might make it desirable to store hydrogen, produced in the desert, for example, as methanol for easier storage and shipping.

We are concerned with the chemical reaction

$$CO_2 + 3\,H_2 \rightarrow CH_3OH + H_2O$$

and its characteristics and parameters. This reaction is exothermic but only takes place if a suitable catalyst is used. The catalyst only works well at high temperatures (200°C-300°C) and the reaction itself favours high pressures. It is our goal to test a number of catalysts and find the optimum working parameters.

In this article we report on some measurements made with a catalyst developed at the Laboratory for Technical Chemistry at the ETH in Zurich. The catalyst is made of a copper particles on a zirconia support [2].

In Fig. 1 we show measurements of the conversion of CO_2 to methanol as a function of the catalyst temperature at a pressure of 30 bar. The initial gas consisted of one part CO_2 and three parts H_2. The catalyst used consisted of 4 cm^3 of grains which were 250-500 micrometers in size. The flow rate was kept constant at 300 ml/min (at normal pressure and temperature). Thus the space velocity, i.e. flow rate/catalyst volume, was 4500 h^{-1}.

In Fig. 2 we show the carbon dioxide to methanol conversion as a function of pressure at the temperature of 240°C, amd a H_2/CO_2 ratio of 3.

It is not only methanol which is generated from carbon dioxide and hydrogen but also carbon monoxide, methane, water and other products. In Fig. 3 we show the conversion of carbon dioxide to CH_3OH, CO, CH_4 as a function of temperature.

In Fig. 4 we show the carbon dioxide to methanol conversion as a function of the H_2/CO_2 ratio at a pressure of 30 bar. By increasing the amount of hydrogen the conversion increases only slightly.

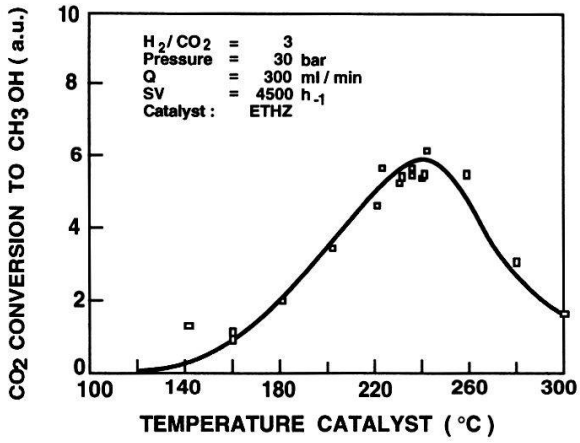

Fig. 1 Conversion of CO_2 to methanol as a function of temperature

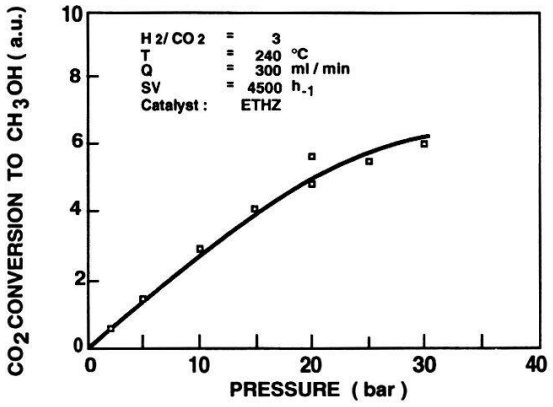

Fig.2 CO_2 conversion to methanol as a function of pressure

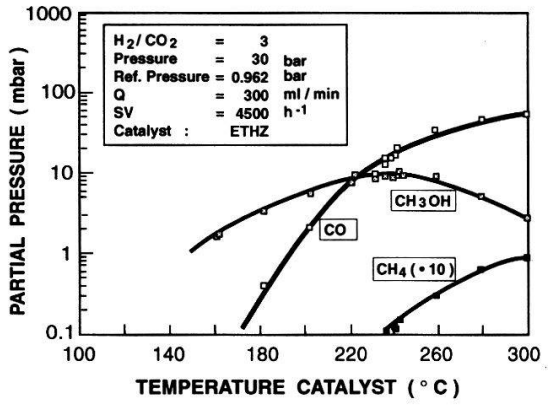

Fig. 3 Conversion of CO_2 to CO, CH_4, CH_3O_4 as a function of temperature

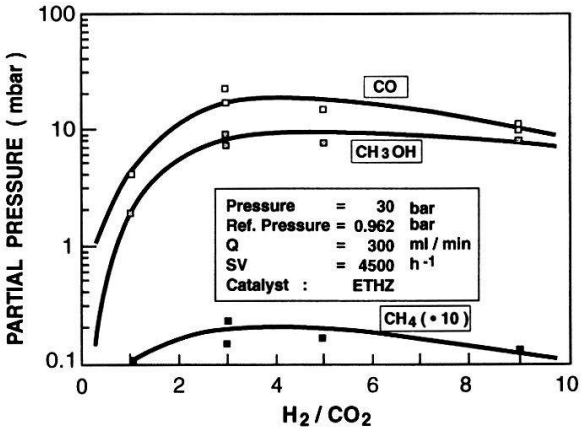

Fig.4 CO_2 conversion as a function of H_2/CO_2 ratio

All measurements were taken by going only once through the reactor and the contact time was only 0.8 seconds under normal conditions.

These measurements are being extended to cover other catalysts. An important question to be answered is the effect of small amounts (ppms) of trace gases in the original carbon dioxide supply on the lifetime of the catalyst.

[1] B. Eliasson, "CO_2 Chemistry. An Option for CO_2 Emission Control?", CO_2 - Chemistry Workshop, Hemavan, Sweden, September 20-23, 1993.

[2] R. A. Köppel, "Strukturelle und katalytische Eigenschaften von Kupfer-Zirkondioxid Katalysatoren für die Synthese von Methanol aus Kohlendioxid und Wasserstoffî", Dissertation Nr. 9347, ETH, Zürich, 1991.

UNDERSTANDING PROBLEMS FROM 'REAL LIFE' WITH COMPLEX FLUID PHYSICS: BIOCOLLOID STABILITY AND AGGREGATION

S. U. EGELHAAF, H. H. BAUER[§], H. P. MERKLE[§], and P. SCHURTENBERGER*
Labor für Elektronenmikroskopie 1, [§]Galenische Pharmazie,
*Institut für Polymere, ETH Zürich, CH-8092 Zürich, Switzerland

Although human calcitonin (hCT) is a potential drug, an everyday administration of hCT solutions is impossible because hCT aggregates within a short time. To understand the aggregation process in more detail, we investigated the dominating interparticle interactions by static (SLS) and dynamic (DLS) light scattering experiments, which were analyzed using concepts from the theory of complex fluids.

The peptide hormone calcitonin keeps the calcium concentration in the blood on a constant level by controlling its elimination by the kidney and its fixation in the bones. It could also be used as a potential drug against several diseases, such as osteoporosis, hypercalcemia, or Paget's disease. However, an everyday administration of hCT solutions is currently impossible, because hCT aggregates and forms a gel within a short time. Therefore hCT solutions must be stabilized to enable a general and easy application of the drug.

The aim of this study is to understand the dominating interparticle interactions, which lead to stabilization or aggregation. They were investigated by SLS and DLS experiments. In a first step the hCT was prepared in a NaCl solution, where the added salt screens the electrostatic interactions between the molecules. Light scattering experiments yield an apparent molar mass M_{exp} and an apparent hydrodynamic radius $R_{h,exp}$ of the hCT molecule, which are in very good agreement with the values expected from the chemical composition of the hCT molecule (M_0, $R_{h,0}$) taking into account hard core interactions on the level of a virial expansion.

In a next step no salt was added to the hCT solutions, which already contain a very small amount of salt from the synthesis of the molecule (~7.3 ions/hCT molecule). For these small ionic strength the SLS data yield a M_{exp} which is much smaller than M_0. This is predominantly due to strong electrostatic interactions between the molecules, which lead to a non-random distribution of the molecules in the solution and to a corresponding reduction of the scattered intensity due to interparticle interference

effects. In the presence of interparticle interactions the osmotic compressibility $(\partial\Pi/\partial C)^{-1}$ is given by:

$$N_A\, k_B\, T \left(\frac{\partial \Pi}{\partial C}\right)^{-1} = M_{app} = M_0\, S(0)$$

where S(0) is the structure factor, M_{app} the apparent molar mass, N_A Avogadro's number, k_B Boltzmann's constant, and T the temperature, respectively. The strong interactions due to the low ionic strength and the relatively high volume fractions necessitate the use of rather involved calculations based on the Ornstein-Zernicke equation [1]. Using the hypernetted chain closure relation, a calculation of S(0) can be made without adjustable parameters and yields good agreement with the measured values.

In the presence of repulsive interparticle interactions, the experimentally determined apparent hydrodynamic radius $R_{h,exp}$ is larger than $R_{h,0}$ due to direct and indirect interactions. The apparent hydrodynamic radius $R_{h,app}$ as obtained in a DLS experiment is formally given by:

$$R_{h,app} = \frac{S(0)}{H(0)\, H_{ion}(0)}\, R_{h,0}$$

where $R_{h,0}$ is the hydrodynamic radius in the absence of interactions, H(0) is the indirect (hydrodynamic) interaction term, and $H_{ion}(0)$ takes into account the mobility of the small ions in the solution, respectively. The calculated $R_{h,app}$ [2,3] are also in good agreement with the experimentally determined values.

The quantitative agreement between the measured quantities and the theoretical predictions support the assumed interaction potential consisting of a hard core and screened electrostatic potential. This enables us to describe the interactions between the molecules and to predict the effects of changes in the solution parameters (such as ionic strength, pH, and hCT concentration) on the aggregation, and thereby find possible means to increase the physical stability of hCT solutions.

[1] B. D'Aguanno, R. Klein, J. M. Méndez-Alcaraz, and G. Nägele, In "Complex Fluids", L. Garrido, Ed., Springer (1993), p.149.

[2] B. U. Felderhof, J. Phys. A, **5**, 929 (1978).

[3] L. Belloni, and M. Drifford, J. Phys. Lett., **46**, L-1183 (1985)

Stabilization of Transient Chaos by Noise

Peter Reimann

Limburgs Universitair Centrum, 3590 Diepenbeek, Belgium

We address the escape rate for single-humped maps near the crisis at fully developed chaos in the presence of weak Gaussian noise. A universal scaling law for the rate is derived predicting a stabilization of deterministic transient chaos by noise.

A large variety of problems arising in very different scientific areas can be described by low dimensional nonlinear dynamics [1]. Of particular interest are sudden qualitative changes that can occur in such systems, for instance bifurcations or crises. A realistic description of these highly sensitive phenomena must include the effect of noise.

In this note we consider a one-dimensional dynamics in discrete time n in the presence of multiplicative noise:

$$x_{n+1} = f(x_n) + g(x_n)\,\xi_n \quad . \tag{1}$$

Here, $f(x)$ is a single-humped map of the real axis with a maximum of order $z > 0$ at $x = x^*$,

$$f(x) = 1 + \Delta - b\,|x - x^*|^z + o(|x - x^*|^z) \quad , \tag{2}$$

where Δ is a small parameter, $-1 \ll \Delta \ll 1$, and $b > 0$. Further, $f(x)$ is continuously differentiable everywhere with the exception of $x = x^*$ for $z \leq 1$. The x-scale is chosen such that $f(x)$ has an unstable fixed point at $x = 0$, i.e. $f'(0) > 1$, and $f(1) = 0$. Thus, at $\Delta = 0$ the map undergoes a boundary crisis and shows fully developed chaos [1]. A well known example with $z = 2$ is the logistic map

$$f(x) = 4\,(1 + \Delta)\,x\,(1 - x) \quad . \tag{3}$$

The noise-coupling function $g(x)$ in (1) is required to be non-vanishing at least at one of the points $x = 0$, $x = x^*$, or $x = 1$ and to be continuous and bounded on the whole real axis. The noise ξ_n is given by exponentially correlated Gaussian random numbers of vanishing mean and small variance,

$$P(\xi_n) = (2\pi\sigma^2)^{-1/2}\,\exp\{-\xi_n^2/2\sigma^2\}\;, \qquad <\xi_n\,\xi_m> = \sigma^2\,A^{|n-m|} \quad , \tag{4}$$

where $-1 < A < 1$ and $0 \leq \sigma \ll 1$. In other words, ξ_n represents weak Ornstein-Uhlenbeck noise. The special cases $g(x) \equiv 1$ and $A = 0$ correspond to additive and white noise, respectively.

By means of a novel perturbation-like method [2] about the deterministic problem at the crisis $\sigma = \Delta = 0$ one finds the escape rate k out of the unit interval $[0, 1]$ in the quasi-stationary state

$$k = \rho(x^*)\,\left(\frac{\sigma\,S}{b}\right)^{1/z}\,F\left(\frac{\Delta}{\sigma\,S}\right) \tag{5}$$

$$F(x) = 2\pi^{-1/2} \int_0^\infty y^{1/z} \exp\{-(y-x)^2\}\, dy \tag{6}$$

$$S = \sqrt{2\left\{(1-A^2)g_*^2 + \frac{1-A^2}{f_0^2-1}\left(\frac{g_0 f_0}{[f_0-A]f_1}\right)^2 + \left(Ag_* + \frac{A g_0}{[f_0-A]f_1} + \frac{g_1}{f_1}\right)^2\right\}} \quad , \tag{7}$$

where $\rho(x)$ is the invariant density for $\Delta = \sigma = 0$ and $g_* := g(x^*)$, $f_i := f'(i)$, $g_i := g(i)$, $i = 0, 1$. This result is expected to be asymptotically exact for sufficiently small Δ and σ [2] and indeed compares very well with the numerical simulations shown in Fig.1. For $z > 1$ and $\Delta < 0$ there is an additional condition required for the validity of (5), namely $\sigma \gg |\Delta|^{\frac{z}{z-1}}$ [2]. With this extra condition, our approach overcomes the difficulties of a perturbation theory about $\Delta = \sigma = 0$, as pointed out in [3].

The escape rate (5) has the form of a scaling law [4] with both universal critical exponents and a universal scaling function $F(x)$ for fixed z. Note that $\rho(x^*)$ is globally dependent on $f(x)$, while all the other details of the map and the noise entering the rate are local properties. The scaling law (5) can also be written under the form $k = \rho(x^*)\,(|\Delta|/b)^{1/z}\, G(\sigma\, S/\Delta)$, where the new scaling function $G(x)$ is related in an obvious way to $F(x)$. Closer inspection shows that for any $z > 1$ the function $G(x)$ has a minimum at $x_{min}(z) > 0$ and that $G(x_{min}(z))/G(0)$ monotonically decreases from 1 for $z = 1$ to $1/2$ for $z \to \infty$. Thus, for any $z > 1$ and $\Delta > 0$ sufficiently small noise-strengths σ will lead to smaller rates than in the absence of noise $\sigma = 0$, see Fig.1. In other words, the noise induces a stabilization of deterministic transient chaos.

Financial support of this work by the Swiss National Science Foundation, the Freiwillige Akademische Gesellschaft, Basel, and the Program on Inter-University Attraction Poles of the Belgian Government is gratefully acknowledged.

References

[1] H. G. Schuster, 'Deterministic Chaos', VHC Verlagsgesellschaft, Weinheim 1988.
[2] P. Reimann, to be published.
[3] S. Grossmann, Z. Phys. **B57**, 77 (1984).
[4] F. T. Arecchi, R. Badii, A. Politi, Phys. Lett. **103A**, 3 (1984).

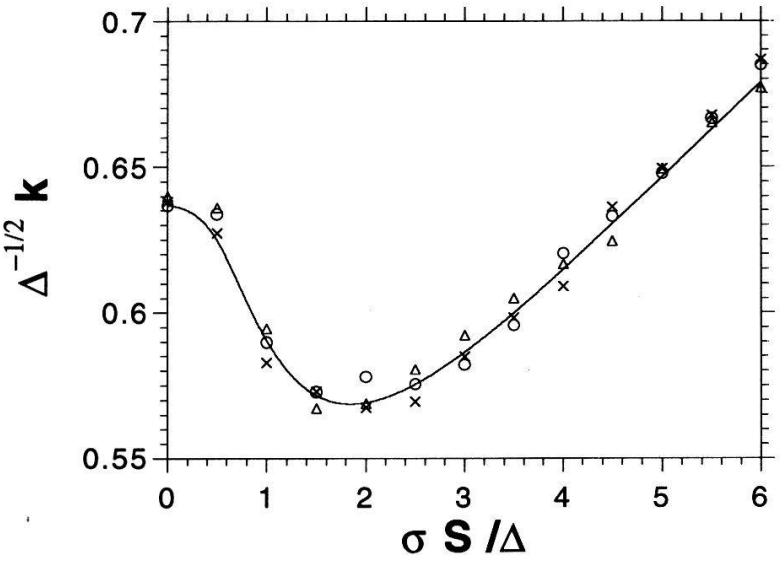

Fig.1: Escape rate k versus noise-strength σ for the logistic map (3) at $\Delta = 10^{-7}$ with additive noise $g(x) \equiv 1$. The curve is the theoretical prediction (5)-(7) with $\rho(x^*) = 2/\pi$ [1]. The symbols are results from numerical simulations of (1), (4) for $A = 0$ (circles), $A = 0.5$ (crosses), and $A = -0.5$ (triangles).